Climate Dynamics (2019) 52:3683–3707
https://doi.org/10.1007/s00382-018-4351-8

Evaluation of multi-decadal UCLA-CFSv2 simulation and impact of interactive atmospheric-ocean feedback on global and regional variability

Jiwoo Lee[1] · Yongkang Xue[2] · Fernando De Sales[3] · Ismaila Diallo[2] · Larry Marx[4] · Michael Ek[5] · Kenneth R. Sperber[1] · Peter J. Gleckler[1]

Received: 21 November 2017 / Accepted: 4 July 2018 / Published online: 13 July 2018

Abstract
This paper evaluates multi-decadal simulations of the UCLA version of Climate Forecast System version 2, in which the default Noah land surface model has been replaced with the Simplified Simple Biosphere Model version-2. To examine the influence of the atmosphere–ocean (AO) interaction on the variability, two different simulations were conducted: one with interactive ocean component, and the other constrained by the prescribed sea surface temperature. We evaluate the mean seasonal climatology of precipitation and temperature, along with the model's ability to reproduce atmospheric variability at different scales over the globe, including extratropical modes of atmospheric variability, and long-term trends of global and hemispheric temperature and regional precipitation. Here, we particularly selected two monsoon regions, East Asia and West Africa, where the simulation of multi-decadal variations which has heretofore been a challenging task, to examine decadal variation of monsoon precipitation. In general, temperature anomaly trends were better captured than those of precipitation in both simulations. Results suggest that the AO interaction, represented as latent heat flux, contributes to improve reproducibility of global-wide climatology, extratropical modes of atmospheric variability, and variability in the multi-decadal climate simulation, as well as for inter-decadal variability of the East Asian summer monsoon.

Keywords Multi-decadal simulations · UCLA-CFSv2 · Atmospheric-ocean interaction · SSiB2 · Modes of variability · Decadal variability

1 Introduction

Significant dramatic decadal climate variability and change have occurred in various monsoon areas during the past century (e.g., East Asia: Li et al. 2004; Ding et al. 2008; Fu et al. 2009; Zhou et al. 2009; Lei et al. 2011; Ha et al. 2012; Yim et al. 2014; Lee et al. 2017; West Africa: Rowell et al. 1995; Mohino et al. 2011; Xue et al. 2016a, b; India: Krishnan and Sugi 2003; Goswami et al. 2006; Han et al. 2014; South America: Zhou and Lau 2001; and many others). Multi-decadal prediction has been one of the most challenging subjects in climate science because of various underlying uncertainties in the natural system's variability under various internal and external forcings and numerical climate models' deficiencies. The prediction of climate variance at multi-decadal and large spatial scales is considered as a forced boundary condition problem; it appears as combined results of anthropogenic effects, natural variability, and external forcings such as volcanic eruptions and the solar cycle, which make the problem more complicated (e.g., Meehl et al. 2009).

Multi-decadal simulation of the historical period (i.e., hindcast) has become a useful way of examining the performance of climate models and investigating the contribution

✉ Jiwoo Lee
lee1043@llnl.gov

1 Lawrence Livermore National Laboratory (LLNL), Livermore, CA, USA

2 University of California Los Angeles (UCLA), Los Angeles, CA, USA

3 San Diego State University (SDSU), San Diego, CA, USA

4 Center for Ocean-Land-Atmosphere Research (COLA) and George Mason University, Fairfax, VA, USA

5 National Center for Environmental Prediction (NCEP), National Oceanic and Atmospheric Administration (NOAA), College Park, MD, USA

of various forcings to climate variability. One of the major key players for the large-scale long-term variance of climate is the ocean, due to its large heat capacity. The ocean serves as a damper and source of climate variance since it stores or releases heat from and to the atmosphere, which lags atmospheric variability but substantially strengthens its inertia. Since the early 1990s, the climate research community under the auspices of the Working Group on Coupled Modelling (WGCM) has established a cooperative effort by designing a standardized experimental setup for the Atmospheric Model Intercomparison Project (AMIP; Gates 1992; Taylor et al. 2012) and the Coupled Model Intercomparison Project (CMIP; Meehl et al. 2007; Taylor et al. 2012; Eyring et al. 2016), which reflects the importance of examining the influence of ocean coupling.

For multi-decadal predictability it is challenging to identify which requisite is more important, either giving an accurate (i.e., prescribed) sea surface temperature (SST) or having proper interaction between atmosphere and ocean (AO) in the model. It would be ideal if both requisites could be satisfied; however, it is not an easy task for climate models. While prescribed SST constrains AO interaction, AO feedback in coupled models could cause bias or drift of the simulated SST. Previous studies endeavored to address this issue by comparing atmospheric general circulation model (AGCM) and coupled general circulation model (CGCM) experiments. For example, Wu et al. (2007) and Kug et al. (2008) suggested that a feedback between SST and precipitation in an AO coupled model contributes to an improved climatology of simulated precipitation. Ham et al. (2014) found that AO coupling improves capturing of climatology, especially precipitation and tropical variance, in their Global/Regional Integrated Model System (GRIMs) (Hong et al. 2013) simulation. Infanti and Kirtman (2017) found that prediction skill and predictability are more influenced by error in forecasted SST field than the AO interaction itself in their Community Climate System Model version 4.0 (CCSM4) simulation. Dong et al. (2017) found that climatology and variance of precipitation is more sensitive to AO coupling than those of surface temperature in the Met Office Unified Model (MetUM) simulation. They emphasized that having AO coupling is crucial for predicting East Asian and Australian monsoons. There are a few recent efforts trying to address both requisites by adjusting ocean fields in CGCMs via data assimilation approaches (e.g., Dong et al. 2016; Lin et al. 2016); however, the majority of climate models are not yet at that stage of development.

The National Center for Environmental Prediction (NCEP) Climate Forecast System version 2 (CFSv2) is one of the most widely used models in the climate prediction and research communities (Saha et al. 2014). Its original version, CFS (Saha et al. 2006), and the upgraded version, CFSv2 (Saha et al. 2014), have been widely used for operational sub-seasonal to interannual predictions (e.g., Yuan et al. 2011, 2013; Mo et al. 2012; Yoon et al. 2012; Jiang et al. 2013; Pokhrel et al. 2016; Pillai et al. 2017; Krishnamurthy 2017), the generation of reanalysis datasets (Saha et al. 2010), and many other research projects (e.g., Kim et al. 2012a, b; De Sales and Xue 2013; Goswami et al. 2014; Pokhrel et al. 2012; Huang et al. 2015; Kumar and Wang 2015; Bombardi et al. 2015a; Sahai et al. 2015; Shin and Huang 2016; Krishnamurthy 2018; and many others). For longer temporal considerations, the NCEP has conducted the CMIP-type runs with the focus on behavioral aspects, such as whether the system is stable or drifting due to assorted technical issues (Saha et al. 2014). The Center for Ocean-Land-Atmosphere Studies (COLA) conducted CMIP5-type decadal climate model simulations (Bombardi et al. 2015b) using CFSv2, but for the set of decadal simulations, individual run were re-initialized every 5 years. Their results suggested that "the reduction of model biases may be the most productive path towards improving the model's decadal forecasts (Bombardi et al. 2015b)". A few studies have conducted a continuous multi-decadal simulations of the CFSv2. For example, Shin and Huang (2016), and Mohan at al. (2018) conducted a 30-year simulations starting from 1980, while Shukla and Kinter (2015) conducted 52-year simulations starting from 1950. They analyzed the climatological annual cycle over the Asian monsoon regions.

The University of California, Los Angeles (UCLA) version of CFSv2 (hereafter referred to as UCLA-CFSv2) has been developed by coupling the Simplified Simple Biosphere Model version 2 (SSiB2; Xue et al. 1991; Zhan et al. 2003) as a land surface modeling component, replacing the Noah land surface model (Ek et al. 2003) that was originally being implemented in the NCEP CFSv2 (Saha et al. 2014). The SSiB2 is a state-of-the-art vegetation biophysical model that preserves energy, water, and momentum conservation at the atmosphere-land surface interface with consideration of the photosynthesis process for surface carbon emission and transpiration (Xue et al. 1991; Zhan et al. 2003). The implementation of the SSiB in the earlier version of the NCEP AGCM, namely the Global Forecasting System (GFS; Xue et al. 2016b), and the UCLA Atmospheric General Circulation Model (AGCM; Arakawa 2000; Mechoso et al. 2000) highlighted the importance of climate–vegetation biophysical processes (Xue et al. 2004, 2006, 2010, 2016a, b; Kang et al. 2007; Ma et al. 2011, 2013a, b), and the impact of dust on the West African, South and East Asian, as well as Amazonian regional climates (Gu et al. 2016, 2017).

This study aims to comprehensively examine the performance of multi-decadal simulations of the UCLA-CFSv2 for 60 years starting in 1949 with focus on assessment of the influence of two-way atmospheric-ocean interaction on global and regional large-scale variance and decadal change. In addition to characterizing the fidelity of the mean state

and modes of variability, we investigate multi-decadal variability on global and regional scales, including for the East Asian and West African monsoons, where significant change of summer precipitation have been observed during the last half century (East Asia: Wang and Ding 2006; Ding et al. 2008; Zheng et al. 2017; West Africa: Rodríguez-Fonseca et al. 2011; García-Serrano et al. 2013; Paeth et al. 2017). This paper is organized as follows: Sect. 2 describes models, observational datasets, and experimental setup; Sect. 3 presents results of the model simulation and its evaluation; and Sect. 4 summarizes the main results with discussions.

2 Data and methodology

2.1 Observations

Multiple sets of reanalysis and observation are being employed in this study. For precipitation, we used the enhanced version of the Climate Prediction Center (CPC) Merged Analysis of Precipitation (CMAP) (Xie and Arkin 1997), 2.5° × 2.5° global monthly version, which is constructed by a combination of surface rain gauge and satellite-derived precipitation estimates, and filled gaps with data simulated from the NCEP/NCAR reanalysis 1 [joint product from the NCEP and the National Center for Atmospheric Research (NCAR)] (hereafter referred to R1) (Kalnay et al. 1996) to provide global coverage. For temperature at 2 meters, we used the Global Historical Climatology Network/Climate Anomaly Monitoring System (GHCN_CAMS) gridded 2 m temperature over land, which provides global coverage of monthly means at 0.5° × 0.5° resolution (Fan and van den Dool 2008). Those datasets are used for the purpose of evaluating simulated mean climatology. We further used the Climatic Research Unit (CRU) time-series (TS) Version 3.22 temperature at 2 meters and precipitation to examine simulated long-term trends. This gauge-based dataset is available at 0.5° × 0.5° horizontal-grid and monthly temporal resolution (Harris et al. 2014). We also used an estimate latent heat flux (LHF) derived from objectively analyzed air–sea fluxes (OAFlux) (Yu and Weller 2007) as reference to compare with model simulated results.

The simulated atmospheric modes of variability are compared against those obtained from the R1. We have analyzed modes of variability using the Common Basis Function (CBF) approach (Lee et al. 2018), which extracts the leading empirical orthogonal function (EOF; von Storch and Zwiers 1999; Xue et al. 2005) modes from the observations and projects them onto the model's anomaly space to avoid complications in selecting the most appropriate model EOF to compare with observations. There is a long history of using this projection approach to analyze modes of variability, including for the boreal winter Madden–Julian Oscillation (Sperber 2004; Sperber et al. 2005), the boreal summer intraseasonal oscillation (Sperber and Annamalai 2008; Sperber et al. 2013), the PDO (Bonfils and Santer 2011), and for ENSO (Bonfils et al. 2015). The CBF approach has also been used for making real-time experimental forecasts of the MJO (Gottschalck et al. 2010), in which forecast anomalies from most of the world's Numerical Weather Prediction models are projected onto the Wheeler and Hendon (2004) observed multivariate basis functions. The major benefits of the CBF approach compared to the conventional EOF approach are: (1) no need to correct arbitrary sign differences of patterns, (2) no need to use EOF mode swapping, which occurs when the model's second or third EOF mode best corresponds to the observed leading mode, and (3) circumventing the potential case in which an observed EOF mode is split across the multiple EOF's modes in a model. In brief, the CBF approach provides a consistent framework to compare how well different models agree with observations. The benefits of using the CBF approach compared to the standard EOF approach for evaluating simulated modes of variability are described in detail in Lee et al. (2018).

2.2 Model and experimental setup

The UCLA version of CFSv2 is comprised of the NCEP Global Forecast System (GFS), the Modular Ocean Model version 4 (MOM4; Griffies et al. 2004) developed from the Geophysical Fluid Dynamics Laboratory (GFDL), and the SSiB2 (Xue et al. 1991; Zhan et al. 2003) as its atmosphere, ocean, and land modeling components, respectively (Fig. 1). We set the spectral discretization of the NCEP GFS at T126 L64, which has about 100 km (about 1°) of horizontal grid spacing with 64 vertical levels; while the MOM4 was set to 0.5° horizontal resolution and 40 vertical levels. For the CFS integrations the ocean and land modeling components interactively feedback and exchange information with the atmospheric component (Fig. 1), while in the GFS integrations only the atmosphere and SSiB2 have two-way interaction, with prescribed SST given by R1 used as the ocean boundary condition (Table 1). Sea-ice input was given by R1.

The experimental design consists of two sets of experiments (Table 1; Fig. 2); spin-up experiments to develop a set of initial conditions for the hindcast simulations, and hindcast simulations that span 1949–2008. The spin-up experiments are discussed in Sect. 3.1, and the hindcast simulations are discussed in Sect. 3.2. During the hindcast integrations, neither re-initialization nor bias correction was applied. All model integrations were conducted on the Stampede supercomputing resource of the Texas Advanced Computing Center (TACC).

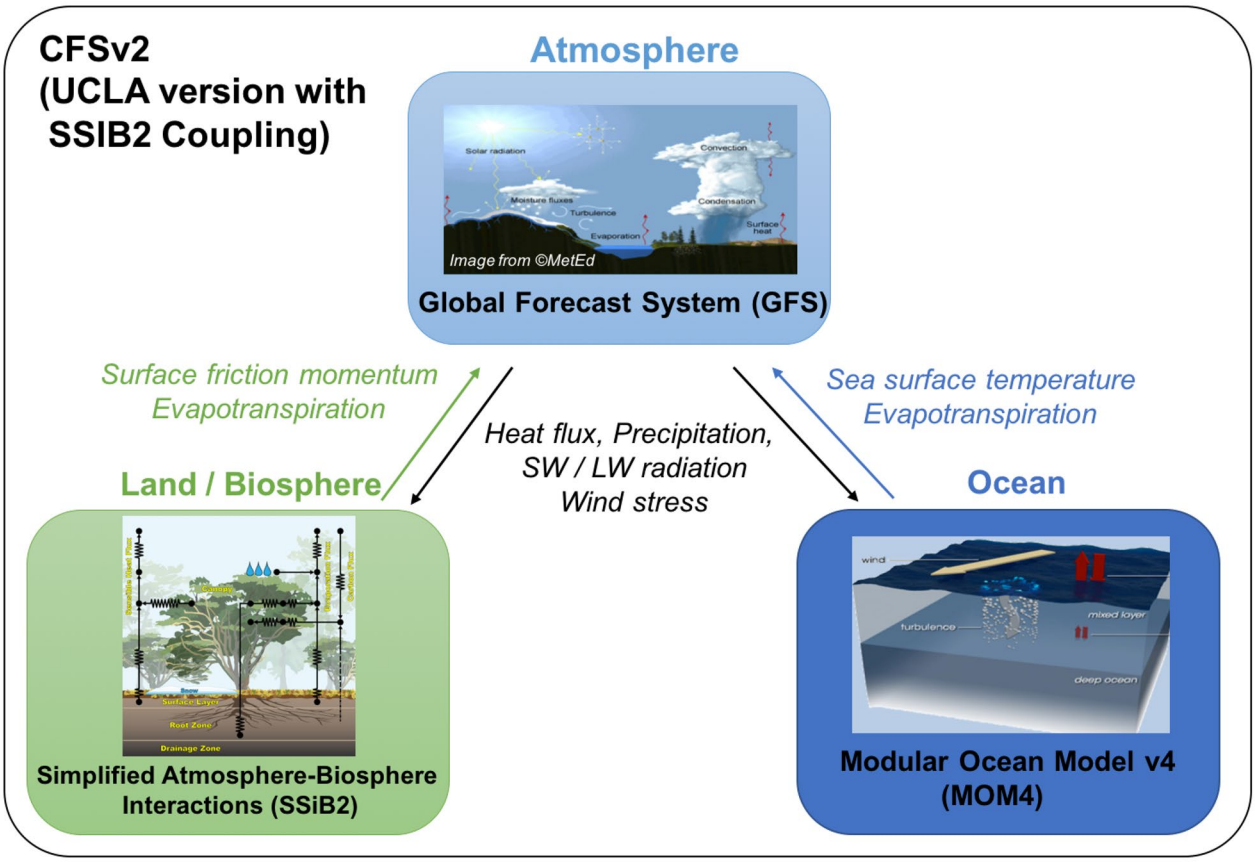

Fig. 1 Schematic diagram for the coupled numerical modeling system, CFSv2. The GFS, SSIB2, and MOM4 are respectively used for atmospheric, land-surface, and ocean modeling components. The arrows indicate ongoing exchange of variables between individual components as during the simulation continues. The schematic image of the atmospheric component is taken from MetEd (https://www.meted.ucar.edu)

Table 1 List of model simulation experiments

Run name	Ocean coupling	Integration period
Initialization (spin-up) run		
CFS_spin-up[a]	Yes	10 years
GFS_spin-up	No (prescribed SST)	10 years
Hindcast run		
CFS	Yes	1949–2008
GFS	No (prescribed SST)	1949–2008

[a]CFS_spin-up is selected as initial condition of both CFS and GFS hindcast runs

3 Results

3.1 Spin-up simulations

We conducted spin-up simulations for the target year, i.e. 1949, using the CFS and GFS (Fig. 2). Since the CFS reanalysis (CFSR; Saha et al. 2010) started from the year 1979, it is necessary to perform spin-up runs to ensure a thermodynamically balanced initial condition for the 1949–2008 simulations. Two approaches for generating the IC's were tested, one with CFS and the other with GFS. In both approaches the initial atmospheric and land surface conditions were for January 1, 1979 from the CFSR, and both simulations were constrained by external forcings (i.e., CO_2 level and solar irradiance) for 1949. The CFS coupled ocean-atmosphere-land spin-up experiment was run for 10 years using as the initial condition of the ocean's three-dimensional thermodynamic structure for January 1949 from GECCO2 (Köhl 2015), the German contribution of the Estimating the Circulation and Climate of the Ocean project (ECCO, http://www.ecco-group.org). In the GFS spin-up experiment the annual cycle of 1949 SST that was used for R1 was prescribed, and repeated for a total of 10 years of integration time. While the atmospheric initial state adjusts quickly, the 10 years of spin-up allows the land surface (and in the case of CFS, the upper ocean state) to stabilize. Based on the comparison of the fidelity of the CFS and GFS spin-up simulations with R1

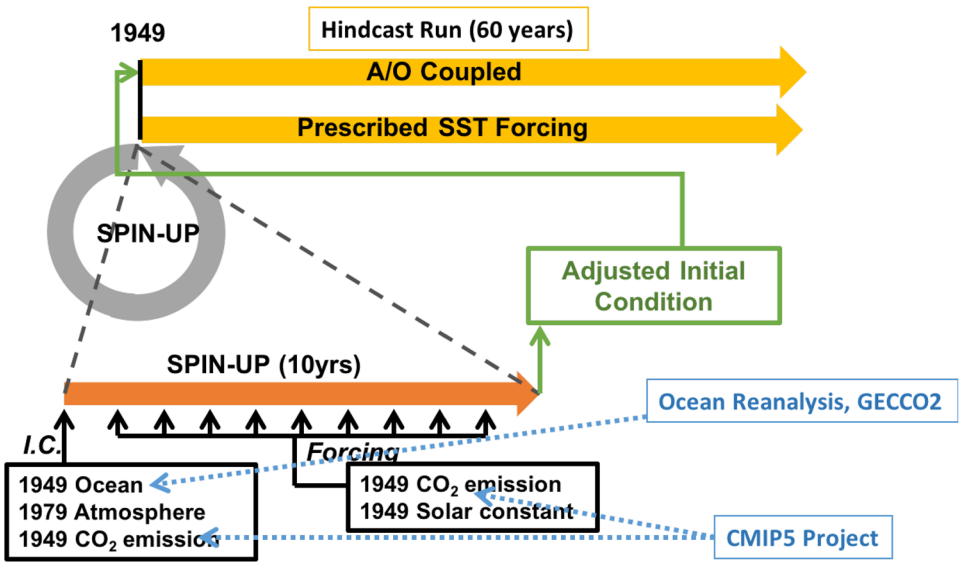

Fig. 2 Experimental setup. We conducted a 10-year spin-up run to have equilibrium model status prior to running the 60 years hindcast simulations. We conducted two types of hindcast simulations using complete CFS components (i.e. atmospheric-ocean coupled) and using GFS (excluding the ocean coupled part and providing prescribed SST from the observation)

Table 2 Time-averaged statistics of the spin-up simulations using CFS and GFS

	PCOR	BIAS	RMSE
200 wind speed			(m/s)
CFS spin-up	**0.87**	**0.30**	**6.21**
GFS spin-up	0.84	1.57	6.59
500 geopotential height			(gpm)
CFS spin-up	**0.69**	**−0.03**	**30.08**
GFS spin-up	0.63	−0.08	31.15
Sea level pressure			(hPa)
CFS spin-up	**0.79**	**0.00**	**2.45**
GFS spin-up	0.72	−0.01	2.74
Precipitation			(mm/day)
CFS spin-up	**0.63**	−0.46	**2.71**
GFS spin-up	0.57	**−0.42**	2.82

Spatial pattern correlation (PCOR), bias, and root-mean-square error (RMSE) of seasonal (3-month) mean distribution for each variable against 1949 of Reanalysis-1 (R1) are listed. Statistics are obtained globally but in latitude range of 60S–80N. Highlighted numbers using bold font indicate better performance

(see below), we select the last time step of the 10-year CFS spin-up run, as the initial conditions for the CFS and GFS hindcast simulations.

Table 2 summarizes the statistics for the two spin-up simulations against the target year of R1 dataset. We calculated statistics for the individual seasons of simulation against the corresponding season of the target year in the reanalysis. For example, we averaged 3 months (DJF, MAM, JJA, SON) of model fields for every 10-year simulation. There are 4 snapshots per year per variable, thus 40 snapshots for the entire simulation. The model's output for each season in its 10-year spin-up run was compared to the 1949 seasonal mean of R1. The 200-hPa wind speed differences from CFS_spinup and GFS_spinup with respect to R1 are 0.30 m/s and 1.57 m/s; i.e. the difference for GFS_spinup is more than quintuple that of CFS_spinup, although both pattern correlations (PCORs) exceed 0.83 (Table 2). The 500-hPa geopotential height systematic errors (BIAS) for CFS_spinup and GFS_spinup are −0.03 and −0.08 gpm respectively, which also indicates that GFS_spinup has more than double the CFS_spinup systematic errors. Overall, except for bias of precipitation in Table 2, CFS_spinup shows better performance than GFS_spinup, when both are compared against the 1949 seasonal means of R1.

In view of the encouraging performance of the CFS_spinup, in the remainder of this paper we concentrate on the CFS and GFS comparison of simulated global/regional climate with the CFS_spinup utilized as the initial condition for both the CFS and GFS integrations.

3.2 Historical hindcast simulations

3.2.1 Climatology

The last 29-year (1979–2007) hindcast simulation was selected for analyses of climatological fields because it is the longest common period covered by every observational reference dataset used in this study. We calculated statistics for individual seasons (DJF, MAM, JJA, SON) of simulation against the same period in R1.

Figure 3 shows the observed and simulated seasonal mean 2-m temperature fields, averaged across the 29 years of the simulation, along with their respective biases relative to the observations. In June–July–August (JJA; boreal summer and austral winter) the observation (Fig. 3a) shows the maximum temperatures (30 °C or higher) is located over

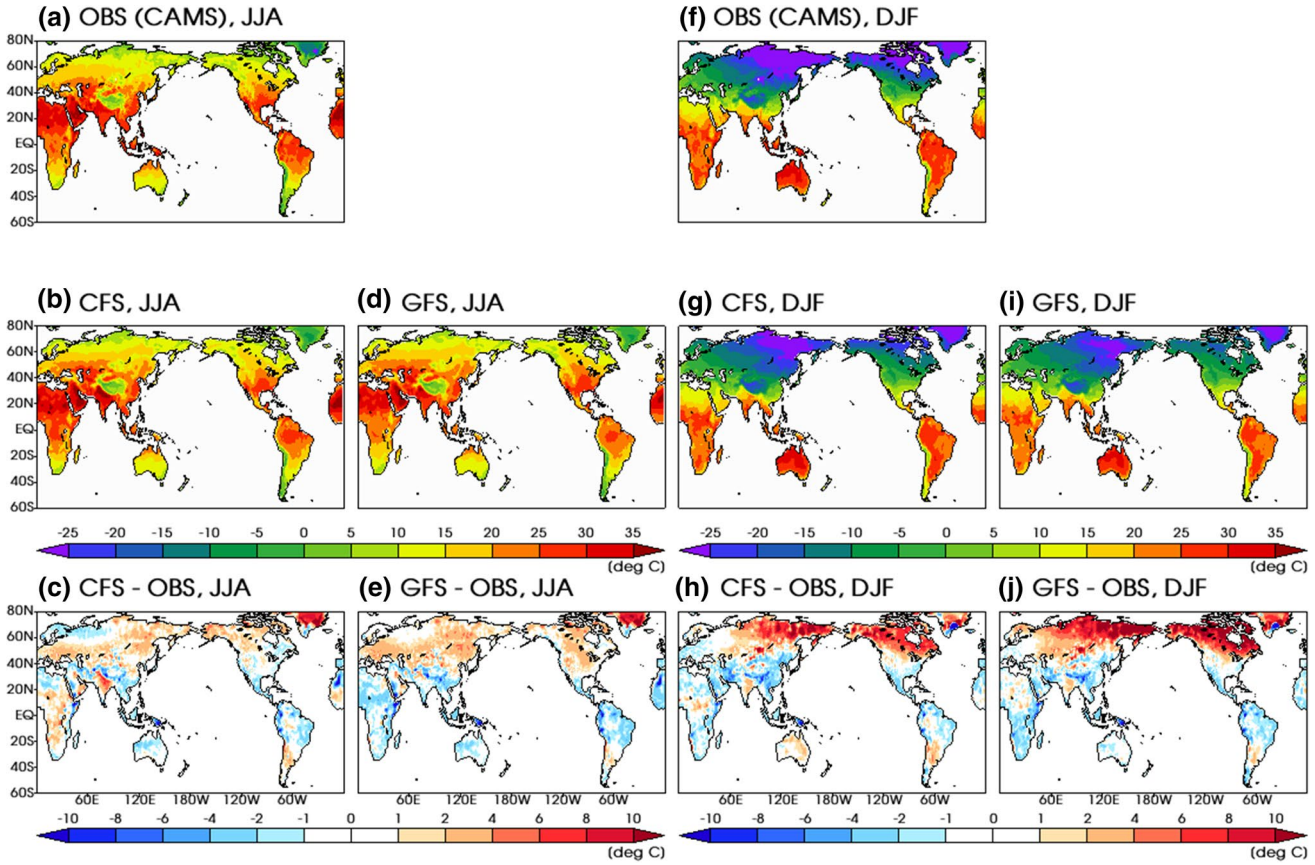

Fig. 3 Seasonal climatology (June–July–August; JJA) of 2-m temperature (units: °C) obtained from **a** CAMS, **b** CFS run, and **c** bias of CFS run (CFS minus CAMS) for the period 1979–2007. **d, e** Same as **b, c** but for GFS run. **f–j** Same as **a–e**, but for December–January–February (DJF) season

northern Africa, the Arabian Peninsula, and the northern part of India, while the lowest temperatures (below zero) are mainly seen over Greenland and the southern part of South America. Both CFS and GFS simulate comparable temperature distribution over the globe (Fig. 3b, d), with pattern correlation coefficients larger than 0.96 (Table 3). The statistics for RMSE are not much different between CFS and GFS (Table 3), being 2.41 and 2.59 °C, respectively, while the corresponding systematic bias errors are 0.16 and −0.2 °C, respectively. Over land the error structure is largely consistent between CFS and GFS, though GFS has a warmer bias (2–6 °C) than CFS over North America and Greenland, while CFS has warmer bias (1–2 °C) over Africa and India, which is not evident from GFS (Fig. 3c, e). Warm bias over North America as shown in GFS (Fig. 3e) is also shown from many other models (e.g., Klein et al. 2006; Ma et al. 2014). Zhang et al. (2018) evaluated models against observation from Southern Great Plains (SGP) site of Atmospheric Radiation Measurement (ARM) Program and showed those warm bias is present in 23 CMIP5 AMIP models.

In austral summer season, December–January–February (DJF), simulated fields from both CFS and GFS runs have high spatial pattern correlation to observation, over 0.98 (Fig. 3f, g, i; Table 3), CFS shows smaller RMSE but larger bias compared to GFS (Table 3). Over land, the structure of the temperature error is very similar in CFS and GFS, though the pronounced warm bias appears in high latitude regions of the northern hemisphere, especially the 60°N region over the Asian and American continents, is stronger in GFS than in CFS (Fig. 3f–j). The warm bias over the southern hemisphere is stronger in CFS than GFS (Fig. 3h, j). Conversely, Saha et al. (2014) found cold biases in high-latitude areas of the northern hemisphere in CFSv2, thus suggesting that the warm biases in Fig. 3h, j are may due to our implementation of the SSiB2 land parameterization. However, it is hard to be sure because direct comparison to result of Saha et al. (2014) is not an available option, which is based on seasonal prediction with some corrections and periodic re-initializations while simulation in this study is a free long term simulation. The majority of the CMIP5 models exhibits similar biases (Lee and Wang 2014), as given by our CFS run. Such cold/warm biases could originate from a variety of factors, including the vegetation distribution,

cloud cover, different ways of representing surface albedo, and partitioning of radiation fluxes (e.g., Xue et al. 2010; Diallo et al. 2014, 2015). Analyzing a 100-year continuous simulation, Swapna et al. (2015) reported that the CFSv2 simulations undergo a rapid cooling reaching a global temperature bias of at least 1.6 °C, which, indeed did not appear in our simulation with SSiB2.

Figure 4 displays the seasonal climatology of precipitation obtained from CMAP observation, as well as simulations of the CFS and GFS, along with respective biases relative to the CMAP observation. In JJA both models capture the dry regions over the Middle East, Southern Africa, Central Australia, and the West Coast of South and North America (Fig. 4b, d). However, there are substantial errors in tropical precipitation, especially in GFS where Maritime Continent precipitation is substantially underestimated (Fig. 4c, e). This result suggests that the Maritime Continent dry bias is not intrinsic to the atmospheric model, but rather it probably arises from the lack of ocean–atmosphere coupling in GFS. This dry bias is consistent to that discovered from results of Shukla and Kinter (2015), who conducted AMIP and CMIP-style simulations using NCEP CFS, and findings of Kang et al. (2002), who discovered underestimated summer monsoon rainfall over the Asia-Western Pacific region in many AGCMs. Wang et al. (2004) argued that lack of the AO interaction may be responsible for this dry bias. The South Pacific Convergence Zone tends to be being too zonal in both simulations. Also, the cyclone track over the Northwest Pacific and Atlantic Oceans appears underestimated in GFS (Fig. 4d). Overall the precipitation pattern is better captured by CFS than by GFS givens its higher pattern correlation, lower bias over land, and smaller RMSE (Table 3).

Concerning monsoons, the CFS has a dry bias over India, which is a well-known problem in the CFSv2 (Goswami et al. 2014; Saha et al. 2014; Silva et al. 2014; Bombardi et al. 2015a; Shukla and Kinter 2015; Swapna et al. 2015; Devanand et al. 2018) and it is consistent with systematic error in CMIP5 models (e.g., Sperber et al. 2013; Li and Xie 2014). In CFS, over India the warm temperature bias is consistent with the underestimate of precipitation (Figs. 3c, 4c). A region of pronounced difference in precipitation between CFS and GFS is over the Gulf of Guinea and the Sahel. In CFS (GFS) there is excessive (deficit) precipitation over the Gulf of Guinea, where the SST is overly warm (see Fig. 5c, f), with deficit (excessive) rainfall over the Sahel. This southward displacement of the convergence zone in CFS is similar to that in other coupled models (Cook and Vizy 2006) which has in part been linked to the overestimate of SST in the Gulf of Guinea (Richter and Xie 2008), as well as errors in the north–south gradient in temperature between the Gulf of Guinea and the Sahara (Roehrig et al. 2013). The CFS wet bias over the northern equatorial tropic region of the Pacific Ocean and dry bias over the northern part of Southern America, the Gulf of Mexico, and East Asia are consistent with the results of Silva et al. (2014), who analyzed the discretized multi decade seasonal hindcast of CFSv2.

Table 3 Statistics of hindcast simulation using CFS and GFS

	PCOR	BIAS	RMSE
Temperature (JJA)		(°C)	(°C)
CFS	**(0.96)**	**(0.16)**	**(2.41)**
GFS	**(0.96)**	(−0.20)	(2.59)
Temperature (DJF)		(°C)	(°C)
CFS	**(0.99)**	(−0.63)	**(3.24)**
GFS	(0.98)	**(−0.03)**	(4.68)
Precipitation (JJA)		(mm/day)	(mm/day)
CFS	**0.84 (0.80)**	0.61 **(0.27)**	**1.86 (1.89)**
GFS	0.78 (0.79)	**0.58** (0.40)	2.05 (1.97)
Precipitation (DJF)		(mm/day)	(mm/day)
CFS	**0.85** (0.80)	**0.64 (0.39)**	1.81 (1.95)
GFS	0.84 (**0.83**)	**0.64** (0.42)	**1.69 (1.65)**
Latent heat flux (JJA)		(W/m^2)	(W/m^2)
CFS	0.91	27.95	37.31
GFS	**0.94**	**25.30**	**33.68**
Latent heat flux (DJF)		(W/m^2)	(W/m^2)
CFS	0.89	26.70	38.38
GFS	**0.92**	**26.18**	**36.29**

Spatial pattern correlation (PCOR), bias, and root-mean-square error (RMSE) of seasonal (3-month) mean distribution against observations (1979–2007; CAMS for 2-m temperature, CMAP for precipitation, and OAFlux for latent heat flux) are listed. Statistics are obtained globally but in range of 60S–80N. Highlighted numbers using bold font indicate better performance. Numbers in () denotes over land only

In the boreal winter season, DJF, both models show qualitatively comparable precipitation distribution against the observation with pattern correlations that exceed 0.8 (Table 3), excepting the tropical Indian and Pacific Oceans the error structure is similar in CFS and GFS, in particular with wet biases over the Pacific Ocean, North America, Eastern Brazil and Southern Africa (Fig. 4f–j). The CFS run has a pronounced double-Intertropical Convergence Zone (ITCZ) problem (Fig. 4g), which is a common issue not only in CFSv2 (Silva et al. 2014), but also in many of modern climate models (e.g., Lin 2007; Hwang and Frierson 2013; Oueslati and Bellon 2015; Zhang et al. 2015; Song and Zhang 2016). Li and Xie (2014) associated this double ITCZ bias with excessive downward solar radiation in the Southern Hemisphere mid-latitudes in climate models. The wet bias over the northern Pacific Ocean and North America and dry bias over Australia and the northern part of South America in the CFS simulation (Fig. 4g, h) are consistent with the result of Silva et al. (2014), as well for JJA (Fig. 4c).

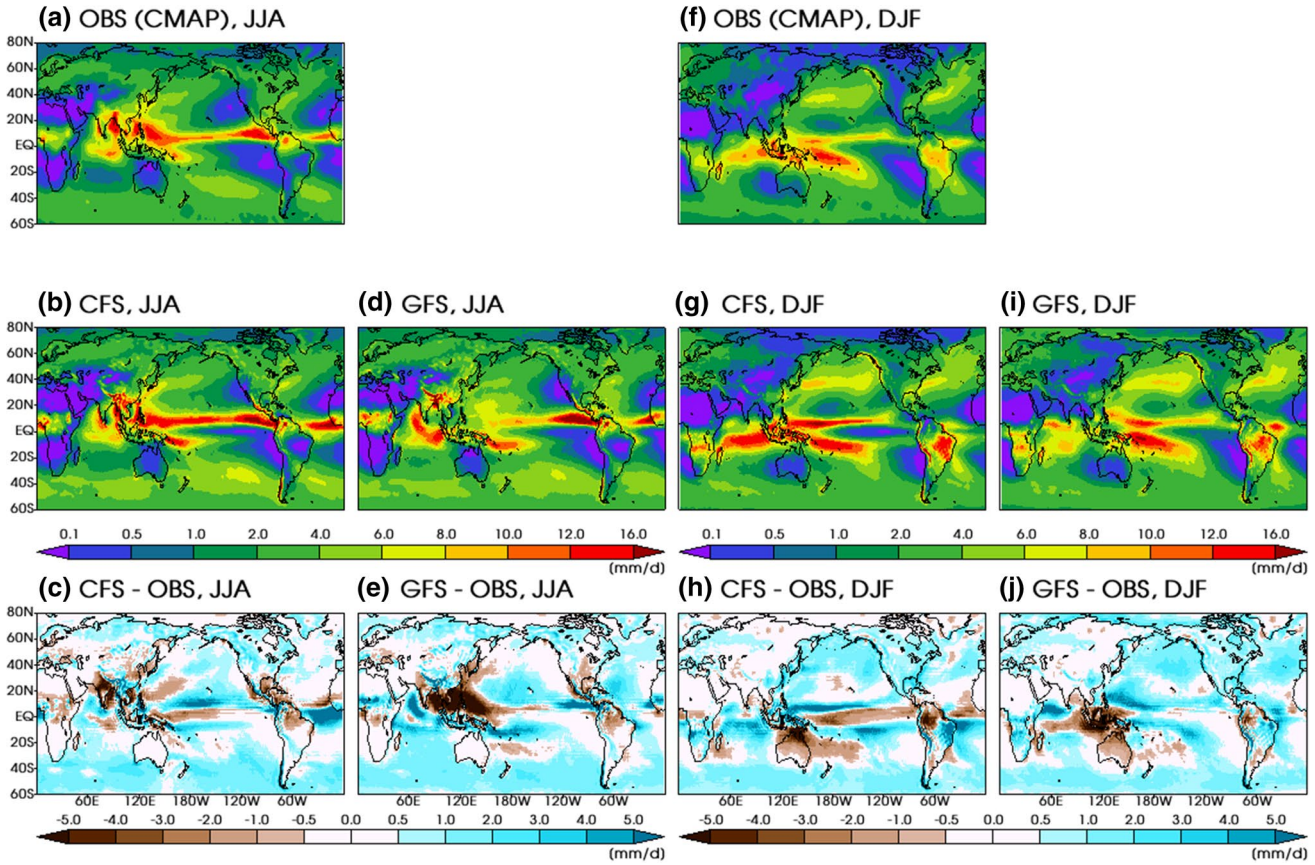

Fig. 4 Same as Fig. 3, but for precipitation (units: mm/day). Observation is obtained from CMAP

The GFS has a wide area of dry bias of 3–5 mm/day over the Maritime Continent (Fig. 4j). This dry bias is not shown in the CFS, which again emphasizes the importance of air–sea interaction for a more accurate simulation of precipitation.

Figure 5 shows comparison of seasonal SST climatology of R1 and CFS, averaged over 1979–2007 period. Since GFS uses prescribed SST obtained from R1, in Fig. 5 we mainly focus on comparing SST from CFS against SST from reanalysis R1. In JJA, CFS has pronounced SST biases over the north Pacific and Atlantic Oceans, also being too warm adjacent to South America, Africa, and near 60°S (Fig. 5a–c). These results suggest that the inconsistencies in the AO coupling do not have significant impact on the mean climate simulation skill of temperature, which is an encouraging point for the GFS simulation (Fig. 3; Table 3). In DJF, CFS ocean shows divided warm area over central tropical Pacific with a colder tongue bias at the equator (Fig. 5e, f), which is comparable to CMIP3 and CMIP5 ensemble average of SST (Zhang et al. 2015, their Fig. 1). This warm bias leads to double ITCZ bias in precipitation (Fig. 4). In CFS, other than the double ITCZ related SST bias, the structural error in SST during DJF (Fig. 5f) is consistent with that in JJA (Fig. 5c). A field of standard deviation obtained from annual cycle removed monthly mean SST shows comparable pattern between R1 and CFS (Fig. 5g, h); but with larger variance (i.e., square of standard deviation) appearing over equatorial Pacific, Northwest Pacific, and Atlantic Oceans. The variance is however overestimated by CFS over tropical Pacific, Indian and Atlantic Oceans (Fig. 5i).

Figure 6 shows observed and simulated latent heat flux (LHF) seasonal means. The LHF plays important role in AO interaction by exchanging heat between ocean surface and bottom atmosphere. Both CFS and GFS models show comparable pattern to the observation with high pattern correlation over or around 0.9 for both seasons (Fig. 6; Table 3). The overestimation is particularly noticeable over the Pacific and southern Indian Oceans in JJA (Fig. 6a–c), and over the northern Pacific in the tropical region (Fig. 6d–f). Table 3 reveals that in general, statistical values of pattern correlation, bias and RMSE for simulated LHF against observation are better for GFS than those of CFS.

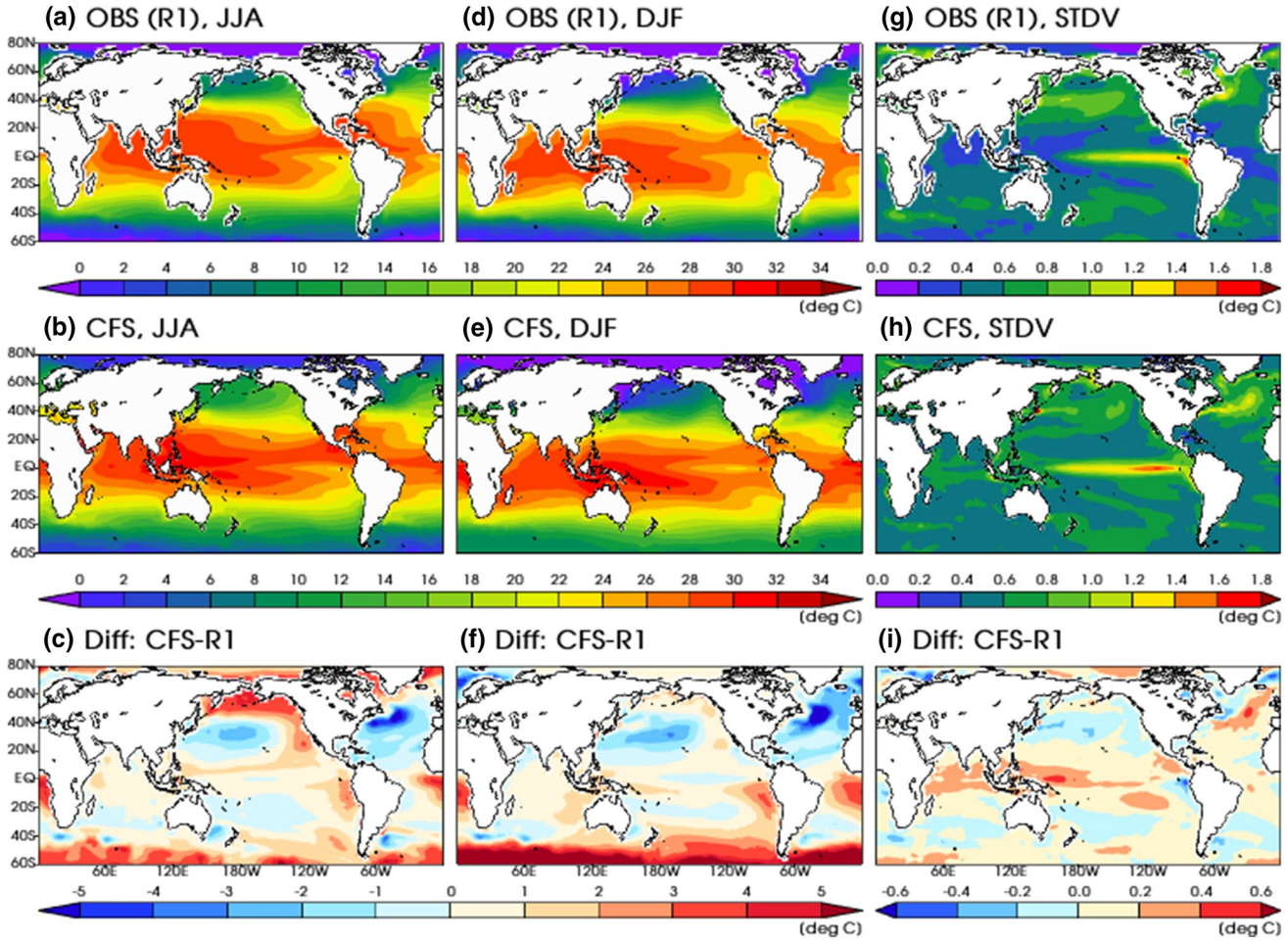

Fig. 5 Sea-surface temperature (SST) of seasonal climatology for 1979–2007 [JJA (left) and DJF (center)] obtained from Reanalysis-1 (R1) (top) and CFS simulation (middle), and differences between them (bottom). Rightmost column is for standard deviation of annual cycle removed monthly anomaly of SST. Unit: °C

In order to investigate the impact of LHF on updraft, Fig. 7 shows differences of seasonal means of LHF (Fig. 7a, b) and vertical velocity at 500 mb (Fig. 7c, d) between CFS and GFS. Note that model returns omega in Pa/s unit for vertical movement, it was then converted to vertical velocity in m/s unit. Increased LHF in CFS over the western Pacific warm pool in JJA (Fig. 7a) favors increased updraft (Fig. 7c), where GFS has significant dry bias (Fig. 4e). Similarly, increased LHF in CFS over the tropical Indian Ocean in DJF (Fig. 7b) induces increased updraft (Fig. 7d), coinciding with regions where GFS has dry bias (Fig. 4j). Those dry biases were indeed relieved in CFS (Fig. 4b, g). Overall, Fig. 7 indicates that the improvement of simulated precipitation was induced by enhanced updraft due to increase of LHF over each ocean area.

To help understand the biases discussed in the global analyses, in addition to the global features, we also analyze a few major features in the East Asian and West African monsoon areas. Figure 8 shows the mean JJA of 850 hPa wind fields over the East Asian region superimposed to both the mean sea level pressure and precipitation from the Reanalysis-1 (R1), CFS and GFS simulations. The 850 hPa wind field in R1 shows westerly flow over Southeast Asia merging with southwesterly flow over East China, Korea, and Japan following along the edge of the North Pacific High, which can be described by the curved contour line, 1010 hPa, over the Northwest Pacific Ocean (Fig. 8). The CFS simulation captures the southwest monsoon circulation and the westward extent of the subtropical high (Fig. 8b). Conversely, in GFS the southwest monsoon circulation is weaker and it does not extend to the Philippines, and the subtropical anticyclone is rather anemic, especially off of the east coast of China (Fig. 8c). The wind errors in GFS lead to weaker convergence and hereby weaker updraft (see Figs. 7c, 8d), which together are responsible for the dry bias in the area (Fig. 4j).

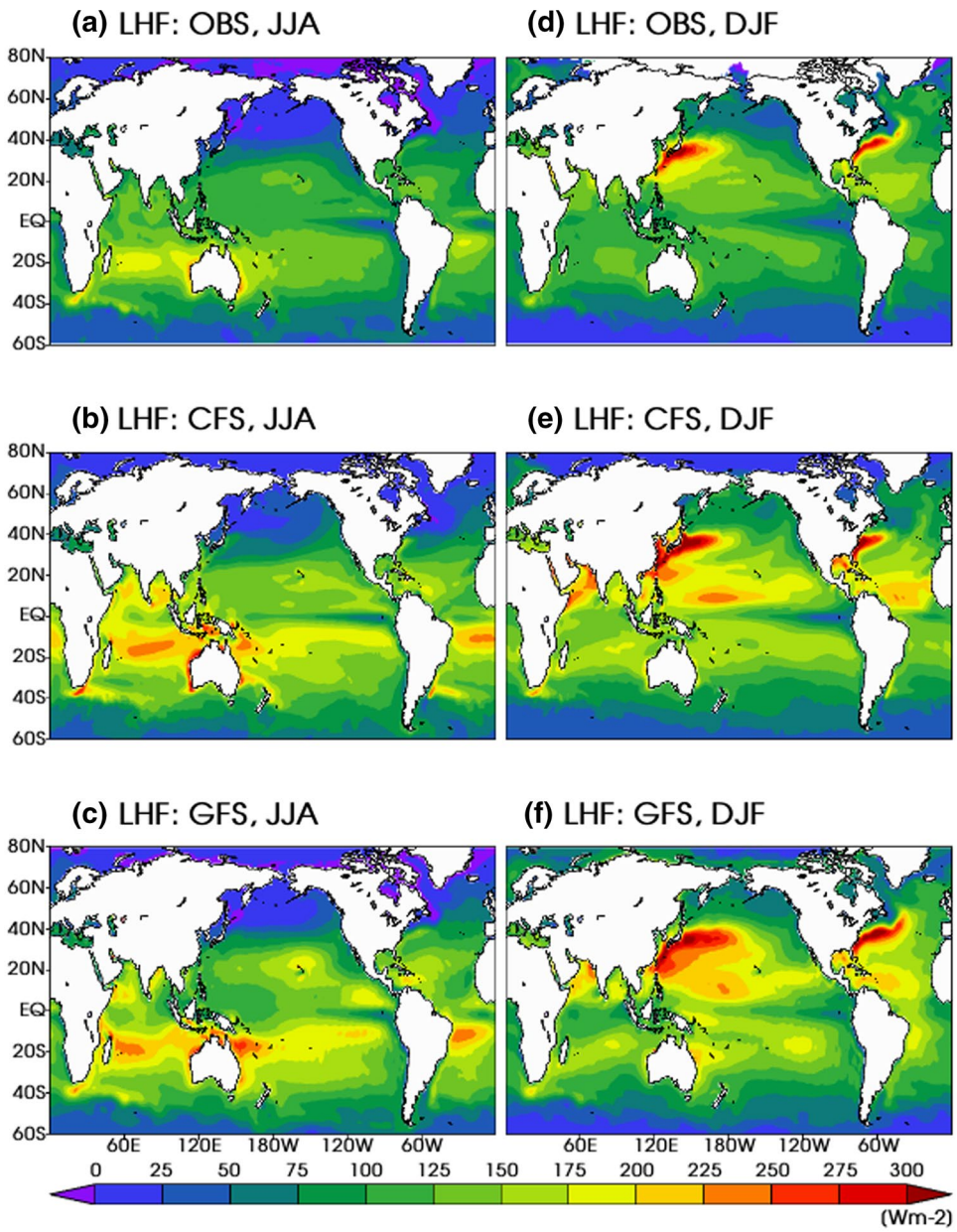

Fig. 6 Seasonal climatology (June–July–August; JJA) of Latent heat flux (LHF) (units: W/m^2) obtained from **a** OAFlux, **b** CFS, and **c** GFS run for the period 1979–2007. **d**–**f** Same as **a**–**c** but for DJF season

Figure 9 is the same as Fig. 8 but zooms in on the West African region. Here we see during in the core monsoon season, June–July–August, the 925 hPa low-level wind field given by the R1 shows easterly flow over the Atlantic Ocean converging along the 10N latitude line, coinciding to area where maximum rainband is located (Fig. 9a). Overall, both CFS and GFS capture the zonally shaped rainband, but the rainband in CFS is further spreaded and shifted to south for about 5° latitude (Fig. 9b–d). High pressure pattern over land is well captured by both simulations while the GFS shows more comparable one than the CFS (Fig. 9b, c). Both simulations has wet bias for precipitation (Fig. 9b, c).

3.2.2 Variability

In this section, we examine simulated variabilities focusing on the latent heat flux (LHF) and extra-tropical modes of variability. Figure 10 shows map of temporal standard deviation, which was calculated from monthly LHF time series of each grid after annual cycle was removed. Thus the figure shows magnitude of monthly LHF anomaly variability. LHF variance is strong over mid-latitude ocean areas, particularly over western Pacific and western Atlantic along the trajectory of ocean current move poleward (Fig. 10a). Although the CFS captures those strong LHF variance region, the LHF variance is overestimated over the tropical Pacific and Indian Oceans (Fig. 10b, c). In the GFS result, however,

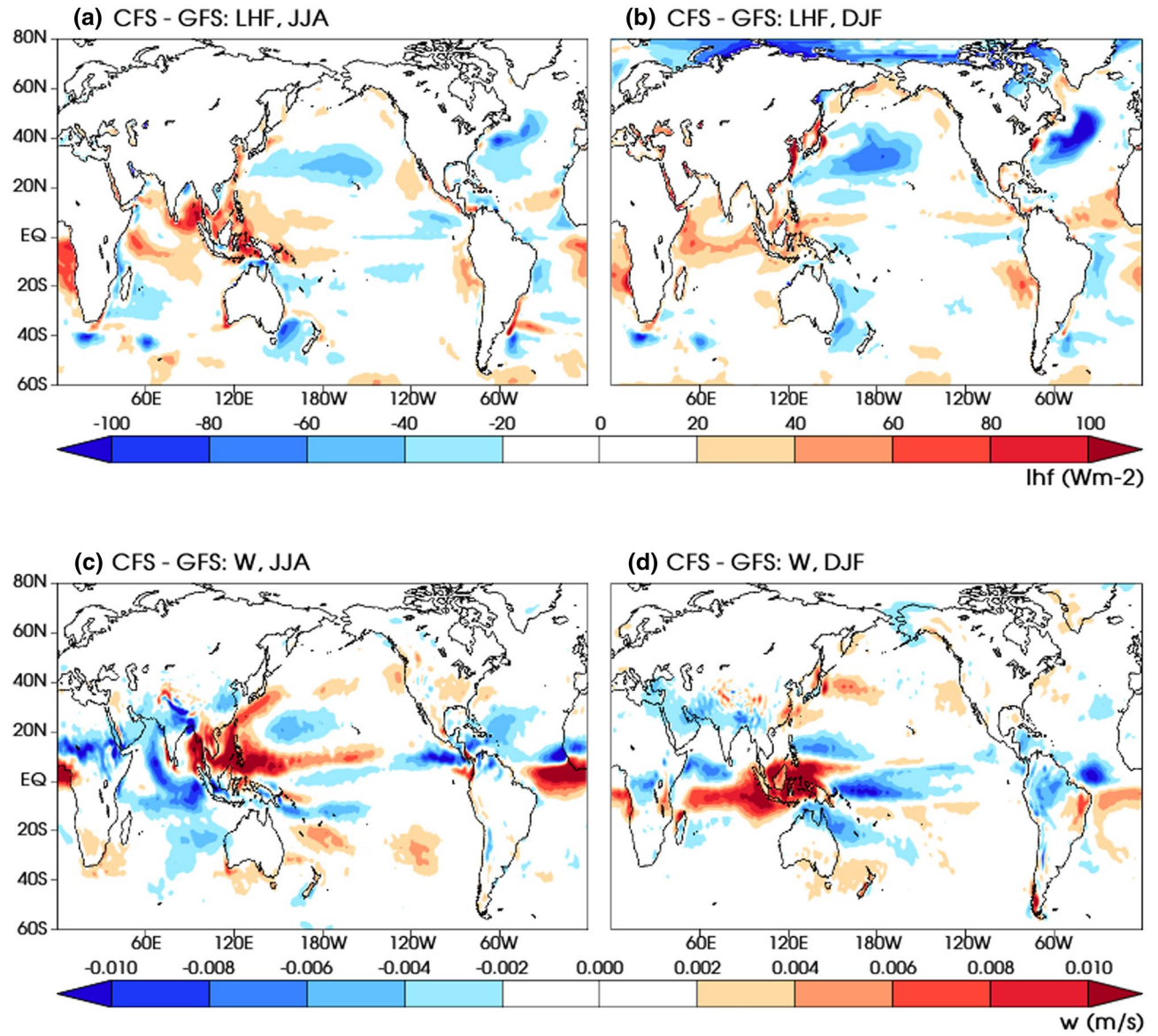

Fig. 7 Difference of LHF between CFS and GFS (i.e., CFS minus GFS; units: W/m^2) for their seasonal average (1979–2007) for **a** JJA and **b** DJF. **c, d** Same as **a, b**, but for vertical velocity at 500-hPa level (units: m/s)

model globally overestimates the LHF variance, where the overestimation is especially strong over the western Pacific, around Maritime Continents, and equatorial eastern Pacific (Fig. 10e).

To further address the time-evolution of LHF variance, we calculated spatial standard deviation values of the map given by Fig. 10 and similar map but obtained from four non-overlapping 7-year period chunks of entire simulation, such as for 1979–1985, 1986–1992, 1993–1999, and 2000–2006 (Fig. 11). The GFS overestimates spatial variance of the LHF's temporal variance while the CFS is more comparable to the observation (Fig. 11). Spread of markers on each bar in Fig. 11 can be considered as an indirect measure of time-evolution. The vertical spreads of markers for OBS and CFS are in similar amplitude, while four markers for GFS are almost overlapped, which means GFS remains too steady to have comparable long-term variation.

Figure 12 is basically similar to what shown by Fig. 10, however, except that the temporal standard deviation is calculated from inter-annual seasonal mean time series anomaly to address long-term variance of LHF, instead of monthly anomaly time series as in Fig. 10. Since Fig. 12 is handling the long-term variance, it is natural that the magnitude of the temporal standard deviation is smaller than month-to-month variance given by Fig. 10. The GFS still overestimates variances in both seasons in global (Fig. 12e, j), like

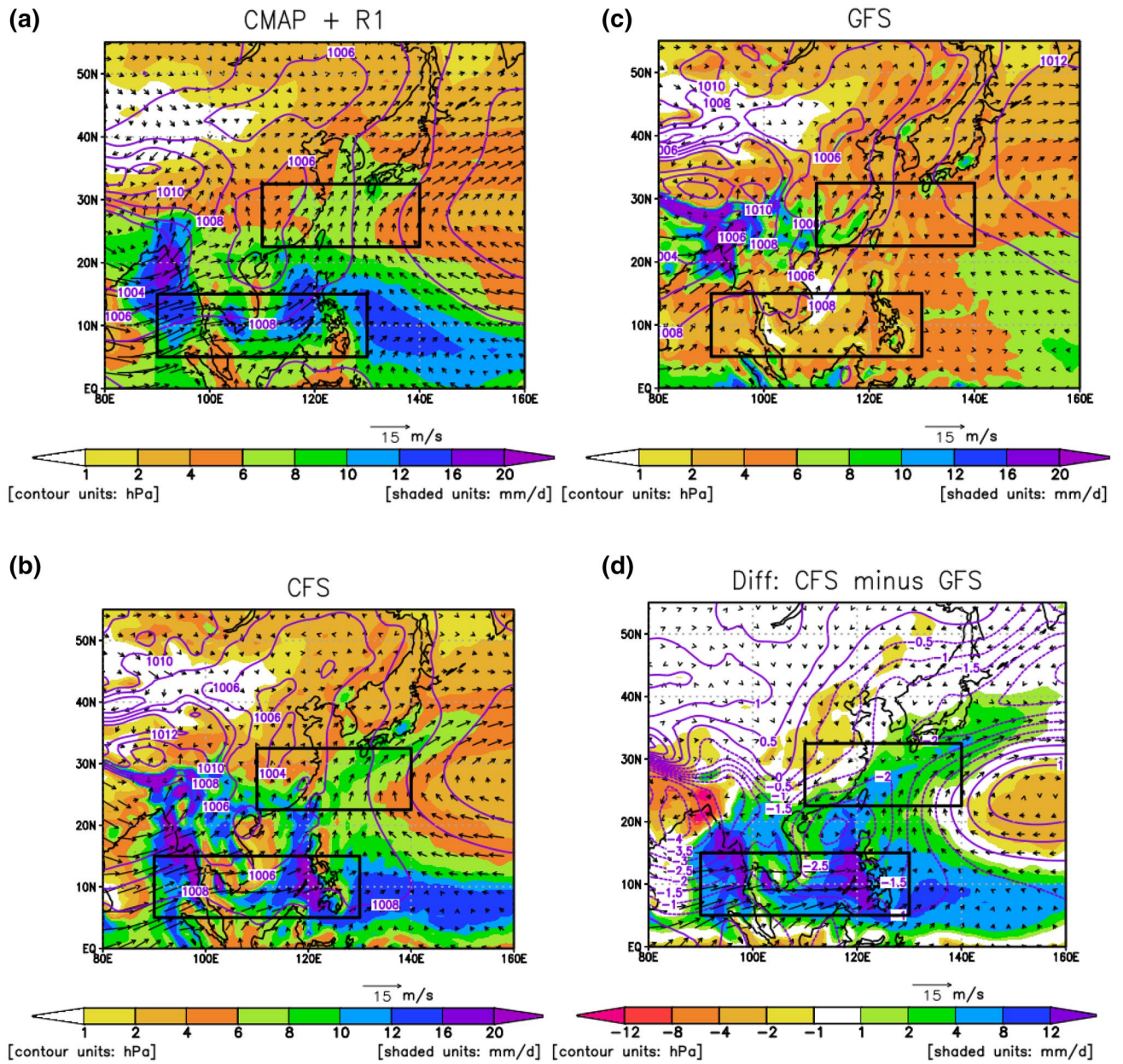

Fig. 8 Seasonal climatology (June–July–August) of sea level pressure (SLP) (contours, hPa), 850 hPa wind (vector, m/s), and precipitation (shaded, mm/day) over East Asia obtained from **a** CMAP (precipitation) and Reanalysis-1 (R1) (other variables), **b** CFS run, and **c** GFS run for the period of 1979–2007. Note that CMAP precipitation is obtained for 1979–2007 by the limited covering period of the dataset. Difference between CFS and GFS models (CFS minus GFS) is shown in **d**. Boxes indicate the averaging area for WF index calculation (Wang and Fan 1999), which will be revisited by Fig. 14

from the monthly variance (Fig. 10). It is distinct that LHF inter-annual variance of CFS shows better agreement to the observation than that of GFS, in both JJA and DJF seasons.

We selected four extratropical variability modes using anomalies of sea-level pressure: the Northern Annular Mode (NAM), the North Atlantic Oscillation (NAO), the Pacific/North American pattern (PNA), and the Southern Annular Mode (SAM). For all modes, we follow the approach of Bonfils et al. (2015) by removing the area-weighted mean over the EOF domain at each time step to remove from the mode of variability any potential regional manifestation due to global-scale climate change. We use the Common Basis Function (CBF) approach, described in Lee et al. (2018) for the analysis of CMIP5 Historical simulations, to get the patterns of simulated modes of variability. In the CBF approach the observed EOF pattern is projected onto a model's anomaly field, resulting in the CBF principal component (PC) time series. Using linear regression between the CBF PC

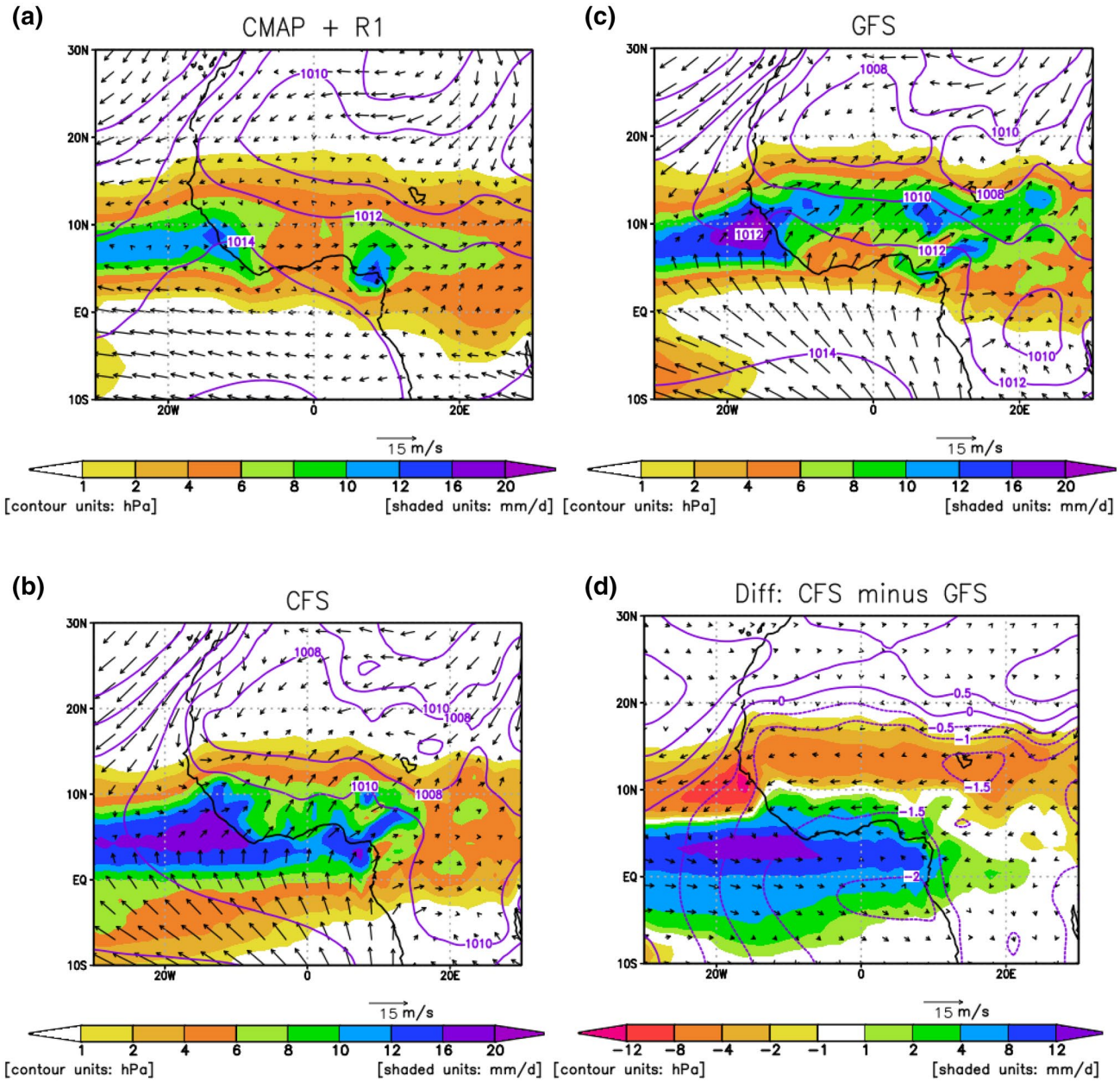

Fig. 9 Same as Fig. 8, but over West Africa with 925 hPa wind vector

time series and the model's anomaly field, the models representation of the observed mode is reconstructed. We use anomalies of DJF sea level pressure from the reanalysis, R1, to obtain the observational leading EOF mode for NAM, NAO, and PNA, while the JJA anomalies are used for SAM. The winter season is selected, since it has the strongest signal in the observations (Lee et al. 2018).

The CFS generates results more comparable to observation than the GFS for NAM, NAO, and PNA (Fig. 13). For NAM, the reanalysis field shows a dipole: one over the polar region and the other over the North Atlantic and Europe (Fig. 13a), which is captured by the CFS although with an overestimated amplitude over the Northern Pacific (Fig. 13b). However, the GFS does not properly capture the intense region over the North Atlantic and Europe, whereas it does capture a false region over the Northern Pacific as CFS does (Fig. 13c). For NAO, the reanalysis shows a distinct contrast between the northern and southern parts of the domain of interest (Fig. 13d). The intensity is reasonably captured by the CFS (Fig. 13e), while it is underestimated in the GFS (Fig. 13f). For PNA, there is a distinguishable region of interest over the Northern Pacific, and

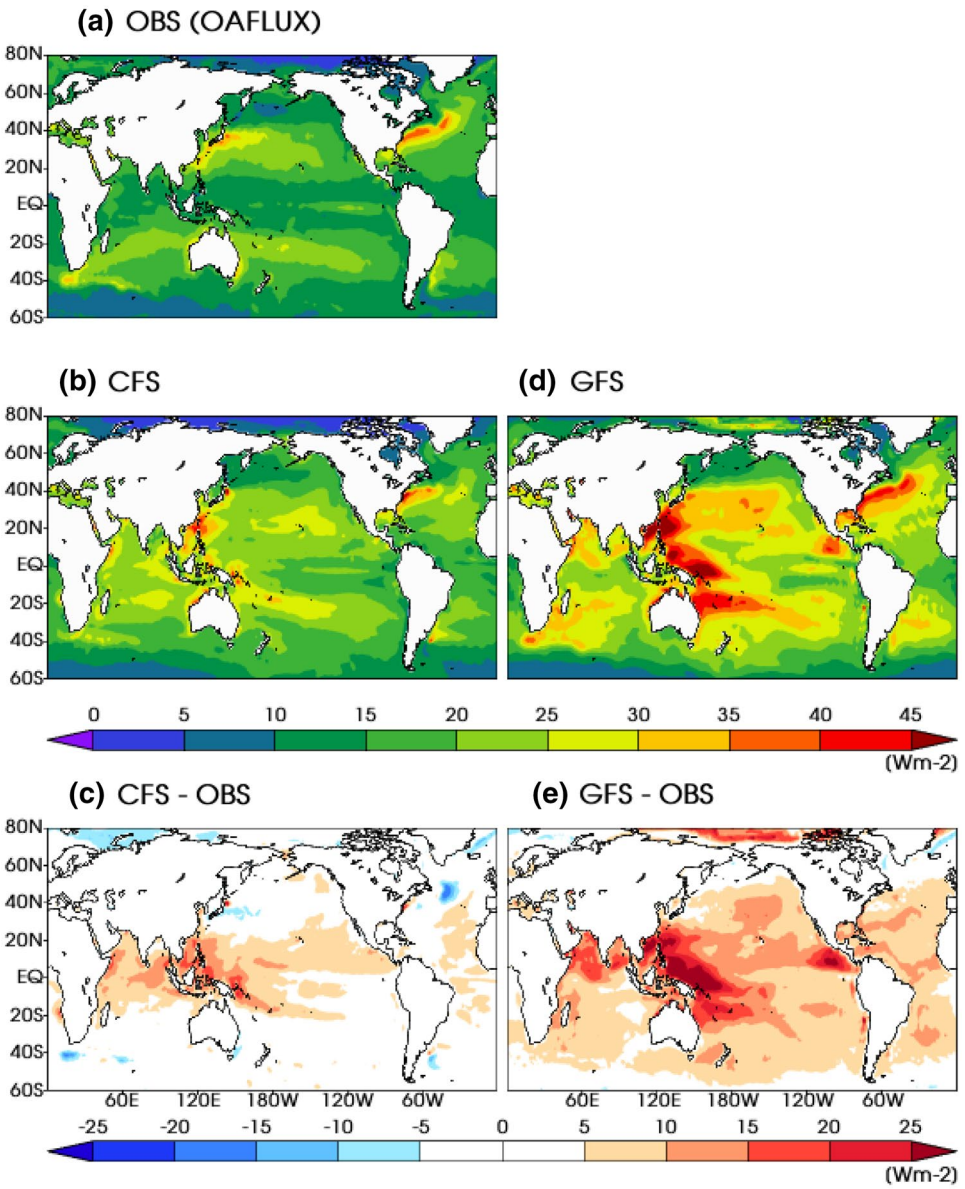

Fig. 10 Map of temporal standard deviation calculated from monthly annual-cycle-removed latent heat flux anomaly (units: W/m^2) time series for each grid point, obtained from 1979 to 2007 of **a** OAFlux and **b** CFS, and **c** their difference (i.e., CFS minus OAFlux). **d, e** Same as **b, c** but for GFS

CFS reproduces it faithfully at its exact location while it is shifted toward the east in the GFS (Fig. 13g–i). While a dipole gradient structure of PNA in GFS (Fig. 13i) is more comparable to R1 (Fig. 13g) than CFS does (Fig. 13h), the shape of bull's-eye-like structure and its location is better captured by CFS. It is supported by statistical values given at Table 4, although GFS gives closer percentage of explained variance to that of R1 than CFS does. For SAM, however, the CFS has weaker variance than observed, whereas the GFS shows better reproducibility (Fig. 13j–l).

We summarized in Table 4, the skill metrics utilized to quantify how well the simulations compare to observations. Our metrics include the pattern correlation (PCOR) between simulated versus observed and RMSE of the simulations. The table also lists the ratio of standard deviations obtained from observed and simulated PC time series, i.e. model/observation—the ideal number should be one. We compared the percentage of variance as well, which represents how much of the total variance is explained by the given pattern. Consistent with the results shown in the spatial map comparison (Fig. 13), the northern hemisphere modes, NAM, NAO, and PNA, are better captured by the CFS than the GFS, while it is opposite for the southern hemisphere mode, SAM, according to the statistical values. It is however arguable that the PNA pattern of the GFS (Fig. 13i) could be more reasonable as the PNA pattern itself indicates

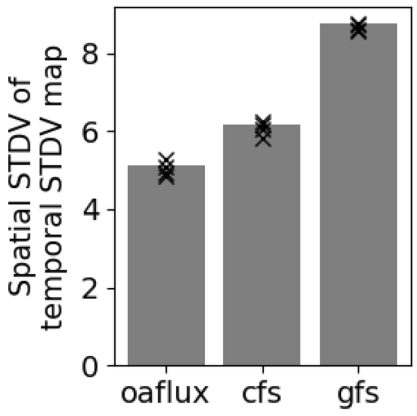

Fig. 11 Spatial standard deviation of the temporal standard deviation map for OAFlux, CFS, and GFS given as Fig. 12a, b, d, respectively (grey bars). The four "x" markers on each bar indicate spatial standard deviation of the temporal standard deviation map as similar to the grey bars but calculated from non-overlapping 7-year chunks (1979–1985, 1986–1992, 1993–1999, and 2000–2006) individually

dipole structure as shown from the reanalysis (Fig. 13g). The improvements for northern hemisphere modes may be related to enhanced capturing of inter-annual variance of seasonal LHF in the CFS (Fig. 12). This indicates that in terms of large-scale atmospheric variance modes, interaction between atmosphere and ocean plays an important role, especially for those modes in the Northern Hemisphere.

We evaluate temperature trends in Fig. 14, which shows the anomaly time series of seasonally averaged land surface temperature over select regions: entire globe, Northern and Southern hemisphere, East Asia, and West Africa. To get those time series, firstly we masked out ocean area so only the land grids were considered. The summer time seasonal mean for each year then was calculated (JJA and DJF for Northern and Southern Hemispheres, respectively), and the anomaly time series over each grid was obtained. We then applied an area average to have a one-dimensional time series and finally applied a 9-year running average to minimize noise and to focus on the major decadal trend. Overall, areas that have an observational temperature increasing trend were well captured by both CFS and GFS experiments (Fig. 14a–e). In general, GFS shows better agreement with observed trends than the CFS. We also selected two monsoon regions; East Asia and West Africa, for further evaluation of regional trends. The temperature trend from the GFS experiment has better agreement with observation than the CFS in terms of temporal correlation and RMSE over East Asia, while that is opposite over West Africa (Fig. 14d, e). GFS shows too much temperature drop in the 1970s compared to the observation while CFS does not show noticeable temperature drop to under the linear trend line (Fig. 14e). We speculate that the significant cold bias of GFS in the 1970s is related to the precipitation, particularly where GFS initiates West Africa drought in the 1980s which was started in the 1970s in the observation (see Fig. 15b).

Figure 15 shows the JJA anomalies variation of precipitation over both East Asia and West Africa. The time series was derived by the same approach as in Fig. 14, but we removed the linear trend to focus on higher frequency variability rather than on the multidecadal trends. Over East Asia, it is clear that CFS follows the observational record better than the GFS (Fig. 15a). During the 1970s, the below average period is well captured by the CFS while the GFS shows the opposite behavior. Over West Africa, the observed drought spans ~ 1970–1993. In GFS the onset of the drought is delayed compared to observations, with the recovery being well-simulated. However, CFS is less realistic, with the onset and termination of the drought occurring too early (Fig. 15b).

To analyze decadal change in detail, we focused on the East Asian region where significant decadal and interdecadal variability of precipitation has been observed (e.g., Wang and Ding 2006; Ding et al. 2008; Zheng et al. 2017). Here, we compared the summer precipitation of averages of the 1980s (1980–1989) and 1950s (1950–1959). Observational analysis shows an increase of precipitation in the middle of Eastern China whereas decreasing occurs over both northern and southern part of East China (Fig. 16a). We examined how models reproduced this difference pattern. Both the CFS and GFS runs captured decrease of precipitation over the southern part (Fig. 16b, c). The CFS run reproduces increasing area over the middle part and decreasing over the northern part (Fig. 16b), whereas the GFS run was not able to reproduce appropriately, but rather displays wet conditions over the northern part of China.

Regarding the interannual analysis of East Asian monsoon, interannual time scales the zonal wind shear index of Wang and Fan (1999, hereafter the WF index) is closely linked to variations of the Meiyu/Baiu/Changma rainband (Wang et al. 2008), with the WF index = U_{850} (5–12N, 100–130E) − U_{850} (20–30N, 110–140E), where presented as boxes in Fig. 8, using JJA averaged data for each year. Figure 17 compares the average and interannual variability of the WF index over the period of 1949–2008 from R1, CFS, and GFS. It is clear that CFS has an average range comparable to the reanalysis, while the GFS underestimates WF index in the overall period, which is caused by failure of capturing the westerly wind over the Southeast Asian region (Fig. 8c, d). The underestimation of the median WF index in GFS is consistent with the misrepresentation of the

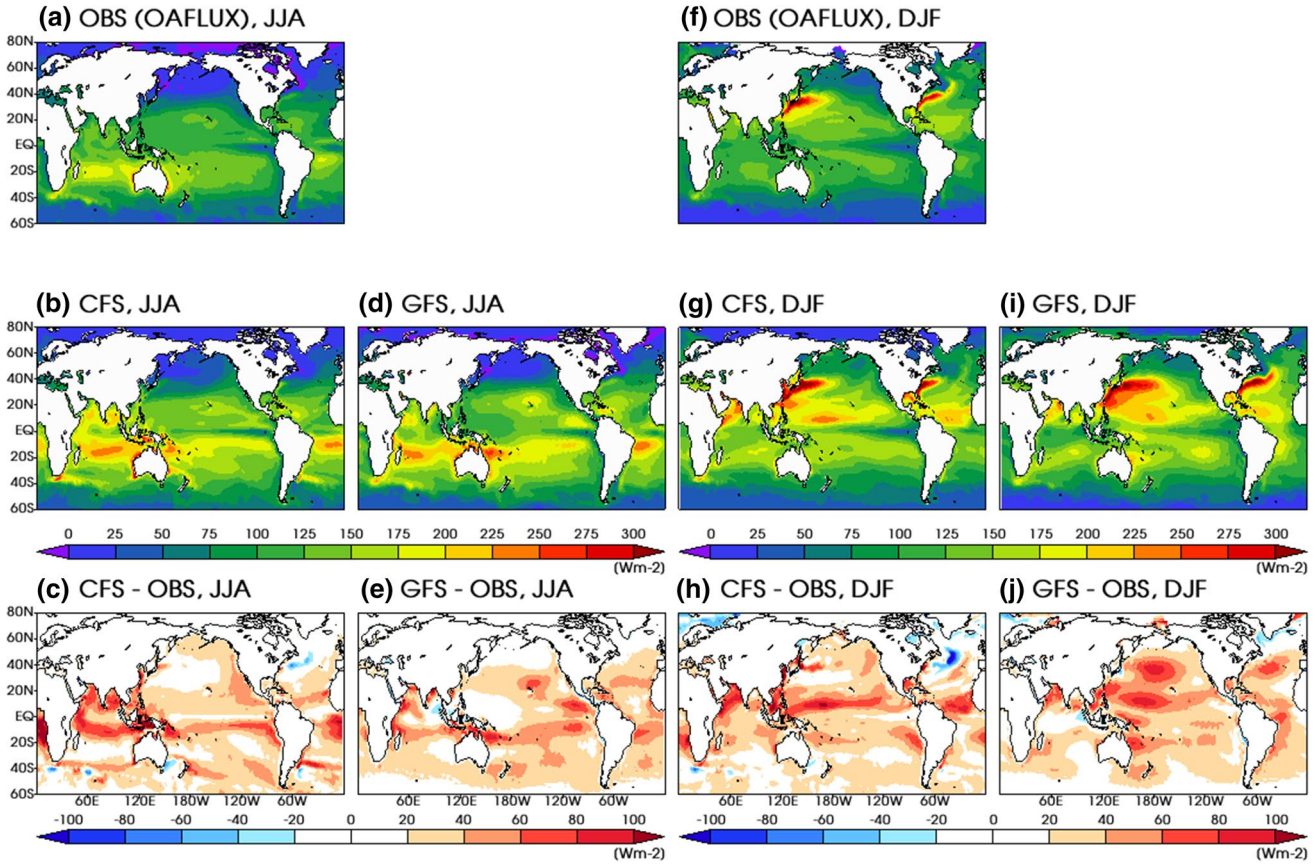

Fig. 12 Interannual variability of seasonal LHF field (unit: W/m^2). **a**–**c** Maps are for temporal standard deviation calculated from JJA averaged latent heat flux anomaly time series for each grid point, obtained from 1979 to 2007 of **a** OAFlux and **b** CFS, and **c** their difference (i.e., CFS minus OAFlux). **d, e** Same as **b, c** but for GFS run. **f**–**j** Same as **a**–**e**, but for DJF season

western Pacific subtropical high (see Fig. 8c), which with weak convergence in turn induces a weak moisture supply, thus resulting in dry conditions over the region (see Fig. 4j). Overall, comparison between GFS and CFS indicates that CFS has more advantage in depicting the atmospheric processes associated with the WF monsoon index (Fig. 17). In agreement with Jiang et al. (2013), our result indicates that the AO is a key element for a reasonable prediction of the East Asian monsoon.

4 Summary and discussion

We conducted multi-decadal hindcast simulations using the UCLA-CFSv2, a branched version of NCEP CFSv2 coupled with the SSiB2 land surface parameterization, and investigated the impact of interactive atmospheric-ocean (AO) feedback on global and regional variability by turning on/off the ocean coupling. To set the initial condition (IC) of the multi-decadal simulation, we conducted a constrained 10-year spin-up simulations in two different ways. After careful evaluation of results of the spin-up simulations, we selected the "CFS spin-up" as the IC to start UCLA-CFSv2 multi-decadal simulations. The UCLA-CFSv2 multi-decadal simulations were conducted in two different ways for its 60-year continuous integration: the "CFS run" is a coupled run using an ocean modeling component, while the "GFS run" is atmosphere standalone run using a prescribed SST given by the reanalysis R1. We evaluated the climatology of temperature, precipitation and latent heat flux (LHF), variability of LHF, atmospheric modes of variability (which are defined with EOF analysis of sea level pressure), and decadal variations of temperature and precipitation over global and selected regional areas.

For climatology, we found the AO interaction plays an important role to advance the model's reproducibility, especially for precipitation. A remarkable dry bias areas of the

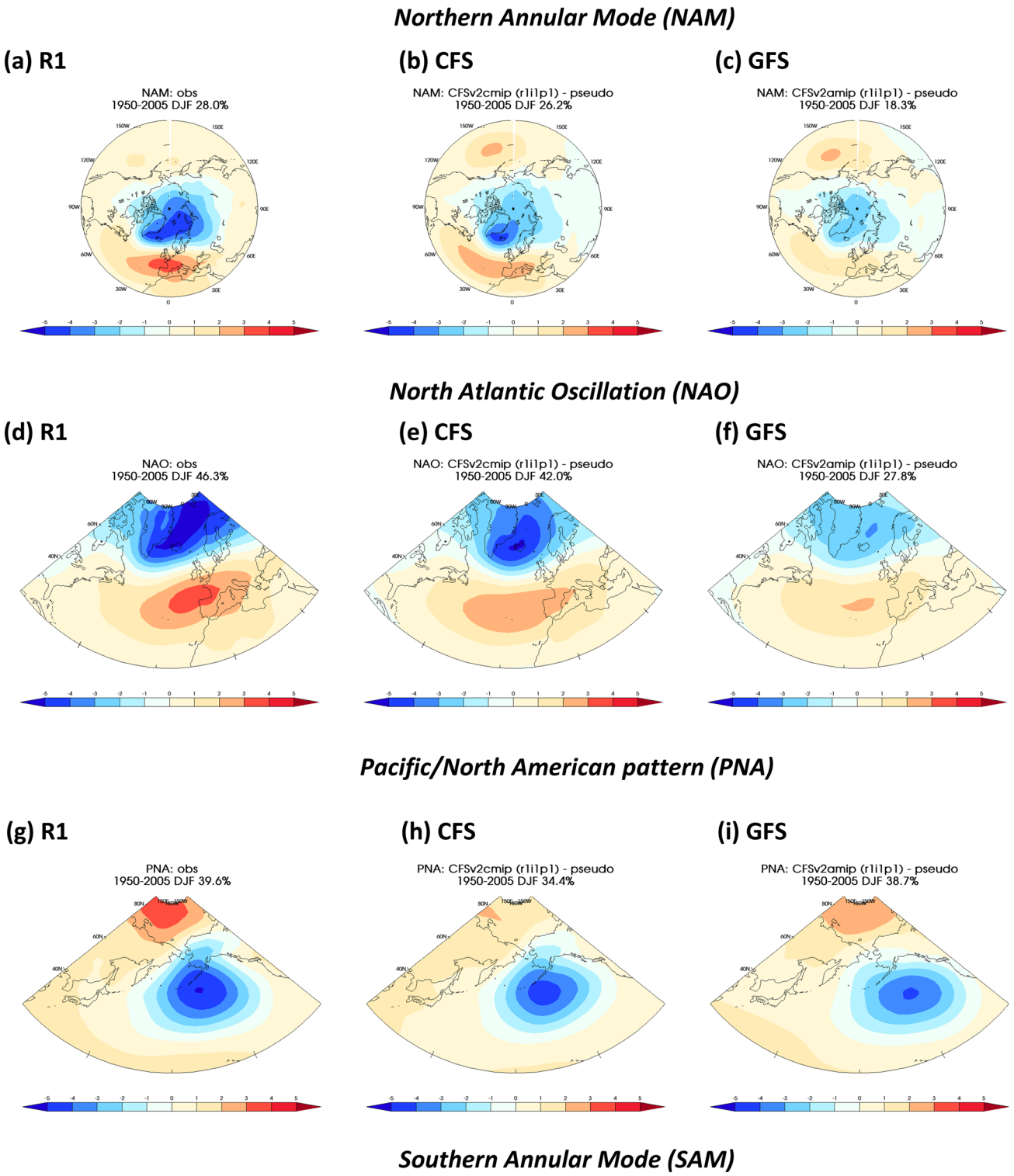

Fig. 13 Pattern of extratropical variability modes, NAM (top), NAO (2nd row), PNA (3rd row), and SAM (bottom) obtained from Reanalysis-1 (R1) as leading EOF (left), and from CFS (center) and GFS runs (right) derived from CBF approach [units: hPa] (continue to next page)

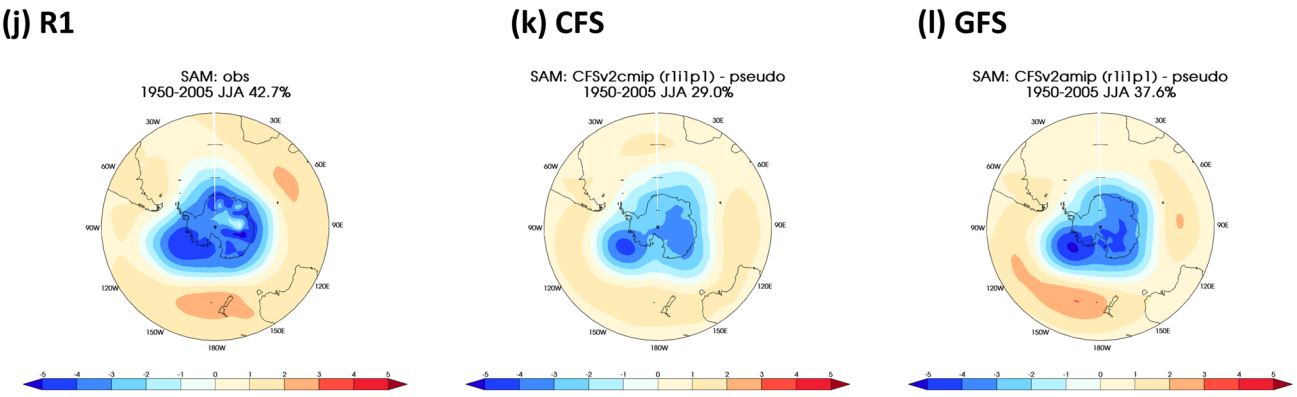

Fig. 13 (continued)

Table 4 Spatial pattern correlation (PCOR), root-mean-square error (RMSE) of map of model's variability mode against Reanalysis-1 (corresponding to Fig. 10), ratio of standard deviation of PC (model/observation; Std_ratio), and percentage of variance explained by the mode (% Var)

Modes	Statistics	Model	
		CFS	GFS
NAM	PCOR	**0.93**	0.89
	RMSE	**0.77**	0.99
	Std_ratio	**0.77**	0.55
	% Var (28.0%)	**26.2%**	18.3%
NAO	PCOR	**0.97**	0.96
	RMSE	**0.74**	1.25
	Std_ratio	**0.83**	0.58
	% Var (46.3%)	**42.0%**	27.8%
PNA	PCOR	**0.98**	0.90
	RMSE	**0.69**	0.81
	Std_ratio	**0.80**	0.74
	% Var (39.6%)	34.4%	**38.7%**
SAM	PCOR	**0.95**	0.94
	RMSE	0.84	**0.71**
	Std_ratio	0.72	**0.83**
	% Var (42.7%)	29.0%	**37.6%**

Note that ideal numbers for PCOR, RMSE, and Std_ratio are respectively one, zero, and one. Reference % Var from the observation is in parentheses. The numbers that are closer to the ideal or reference value are highlighted with bold font

GFS run, over the Western Pacific in JJA and Maritime Continent in DJF, were improved/corrected in the CFS. In fact, enhanced LHF in CFS over those areas increased vertical velocity, consequently causing more precipitation, alleviated the dry biases of the GFS. The alleviation of the dry biases is consistently shown by Jiang et al. (2013) who analyzed 28 years of seasonal and inter-seasonal hindcasts of CFSv2, and Shukla and Kinter (2015) who conducted 52 years of hindcast simulation using CFSv2, in which they compared AMIP- and CMIP-type CFSv2 simulations. The seasonal climatology patterns of precipitation derived by the CFS are comparable to those of Silva et al. (2014). While Silva et al. (2014) evaluated the climatology given by multiple seasonal hindcasts of CFSv2, our result was derived from a continuous multi-decadal simulation without re-initialization during the integration period. This result is encouraging, attesting to the robustness of UCLA-CFSv2. Some common issues of CFSv2 remained in our results, such as dry bias over India (Goswami et al. 2014; Saha et al. 2014; Silva et al. 2014; Bombardi et al. 2015a) and the double ITCZ over the tropical Pacific Ocean (Silva et al. 2014). However, it is worth mentioning that these errors were not amplified in our simulation, which is also encouraging since our simulation is a much longer integration than that of the aforementioned studies.

The SST bias was unavoidable in the coupled run, not surprisingly. However, we also showed variability of LHF in both month-to-month and inter-annual time scales has been significantly improved in the coupled simulation, CFS run. For modes of variability, we speculate that the AO interaction has played a crucial role. We selected four different extratropical atmospheric modes of variability, NAM, NAO, PNA, and SAM. For the northern hemisphere, it is distinct that having AO interaction enhances reproducibility of the variance mode except for the southern hemisphere where having accurate SST field might be contributing more to the reproducibility than the AO interaction.

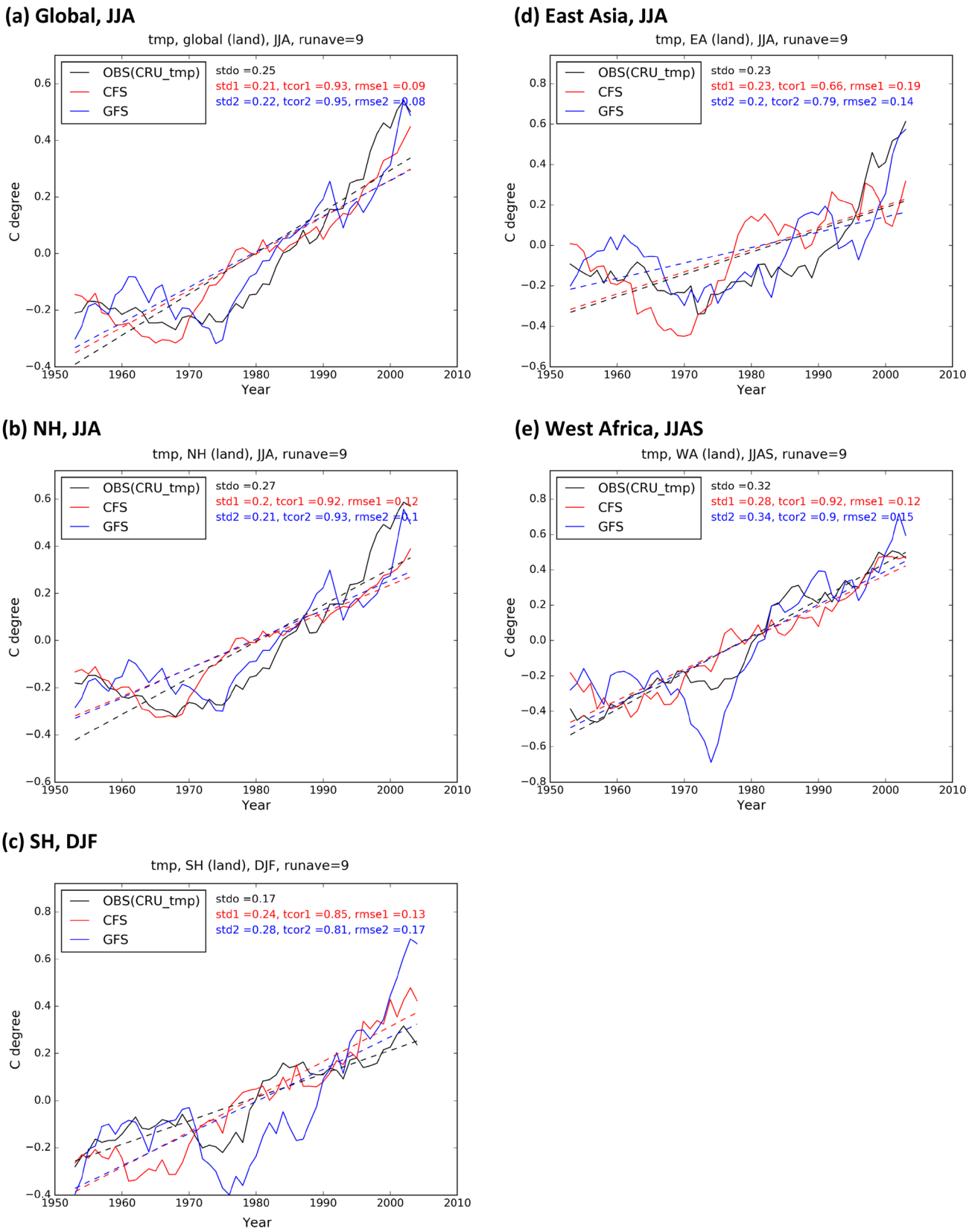

Fig. 14 Time series of 9-year averaged land surface temperature anomaly (units: °C) obtained from CRU, CFS, and GFS for JJA of **a** global (60S–80N) and **b** Northern Hemisphere (EQ-80N), for **c** DJF of Southern Hemisphere (60S-EQ), **d** JJA of East Asia (20–50N, 100–140E), and **e** JJAS of West Africa (10S–30N, 20W–20E)

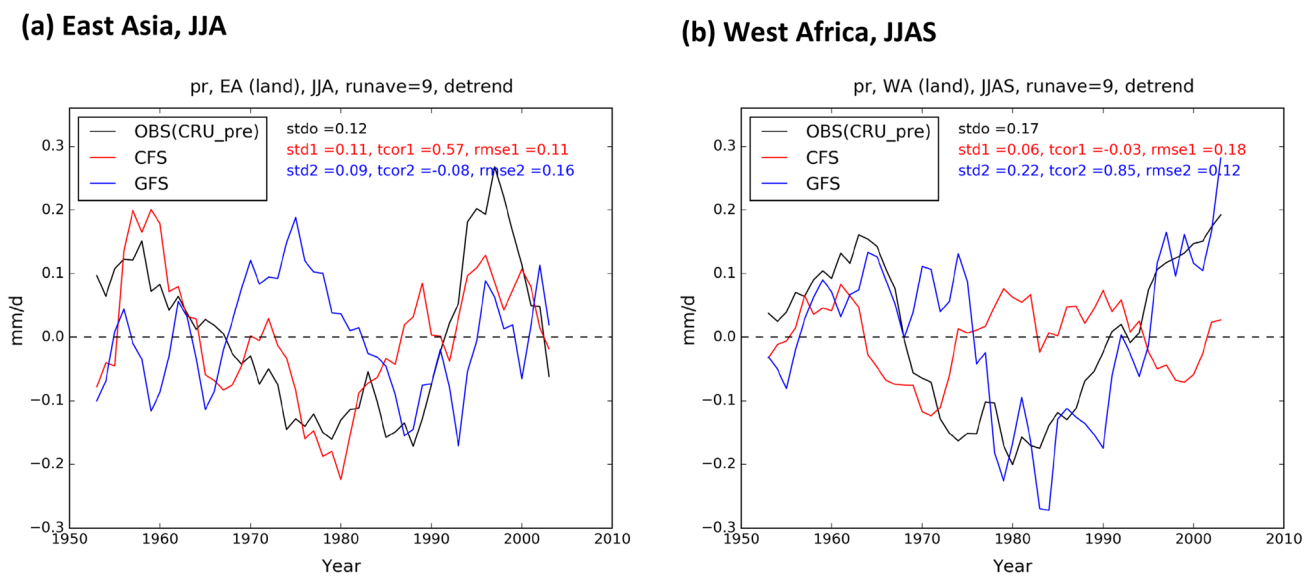

Fig. 15 Time series of de-trended 9-year averaged land precipitation anomaly (units: mm/day) obtained from CRU, CFS, and GFS for **a** JJA of East Asia and **b** JJAS of West Africa

There are two factors that contribute to the proper simulation of the AO interaction: (1) the mean status of the SST, and (2) the processes that contribute to the AO exchange. Our results shows the second process is equally important and is the first order effect that affecting the AO exchange, which has been one of the main purposes to develop the coupled model. Our results suggest that the AO interaction showing as variance of LHF has contributed to improve the performance of multi-decadal climate simulation in terms of climatology (in particular global JJA precipitation and 2-m temperature over land) and modes of variability. Both the CFS and GFS simulations have robustness in capturing increasing linear trend of the observed temperature anomaly. We further focused on East Asian and West African monsoon regions to examine the model's performance in capturing regional trends and decadal changes. The AO interaction is found to be more crucial than the prescribed SST for reproducing inter-decadal variability of the East Asian summer monsoon, while the prescribed SST contributed more to advancing the model's performance for the West African monsoon. The findings for East Asian monsoon are supported by the results of Dong et al. (2017) who highlighted role of AO interaction for East Asian and Australian monsoons by comparing AGCM and CGCM experiments, Zou and Zhou (2013) who argued importance of AO interaction for western North Pacific summer monsoon by implementing partially air–sea coupled model over the area, Song and Zhou (2014) who showed interannual EASM pattern is better simulated in CGCMs than that in AGCMs in CMIP5, and Wang et al. (2005) who suggest that the coupled ocean–atmosphere processes are crucial in the monsoon regions where atmospheric feedback on SST is critical. Note this is only our model's results and more tests with different models are necessary to further study this issue.

There are encouraging point and limitations for this study. The encouraging point is that our UCLA-CFSv2 simulation results is not showing a significant decadal spin-up period associated with a strong global cooling trend, which was occuring in the original CFSv2 (Saha et al. 2014; Swapna et al. 2015). On the other hand, Infanti and Kirtman (2017) presented a contradictory result to ours; they showed prediction skill is more influenced by error in forecasted SST field rather than the AO interaction. More comprehensive investigation is required to determine the factors that produced these differences. Limitations of this study are: (1) detailed regional-scale small features were not much evaluated while we were focusing on a high-level overview of the evaluation, and (2) the study is based on a single member simulation without having ensemble members, which leads the result to be too deterministic. Further currently on-going researches will engage ensemble simulations to consider internal uncertainty of the model. By doing so, we expect we will be at a better position to analyze the leading factor of the decadal change. (3) Analysis for high-frequency (daily or 3–6 hourly) output of model is not included in this study, which has limited clear identification for how AO feedback has improved the model performance. (4) Another source of

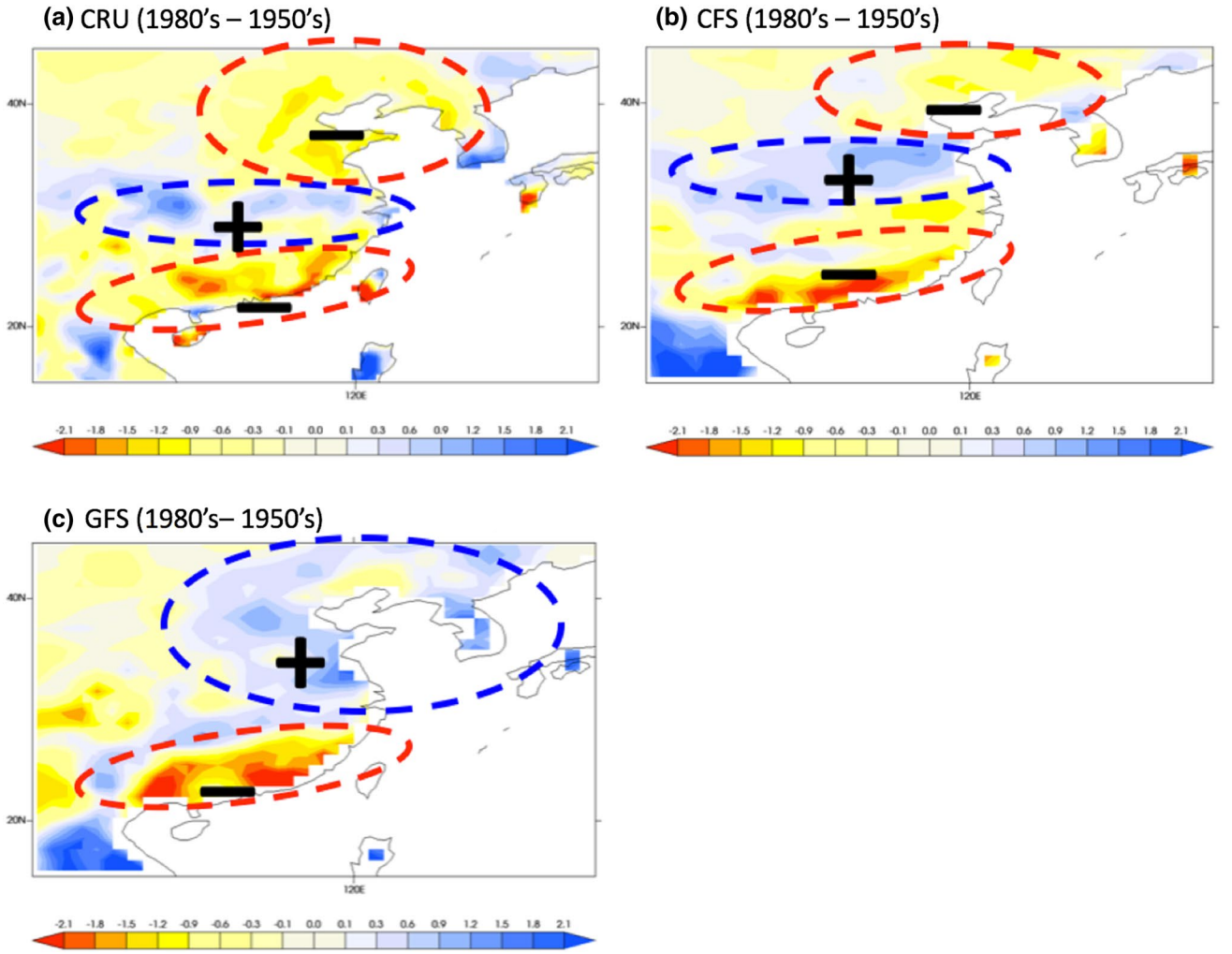

Fig. 16 Decadal change of East Asian summer monsoon (EASM) precipitation: map shows difference of JJA average precipitation (units: mm/day) between 1980s (1980–1989) and 1950s (1950–1959) obtained from: **a** CRU observations, **b** CFS and **c** GFS runs

uncertainty in this study may be caused by the lack of full consideration of aerosols. The East Asian summer monsoon (EASM) region is known to be influenced by aerosol effects, although response to aerosols is highly uncertain (e.g., Guo et al. 2013; Gu et al. 2016; Wang et al. 2015).

Despite limitations, this study is the first to provide an overview evaluation of a continuous multi-decadal simulation of UCLA-CFSv2, with highlights on importance of AO coupling for reproducing appropriate climate variability. Further study will follow, with consideration to overcome the aforementioned limitations.

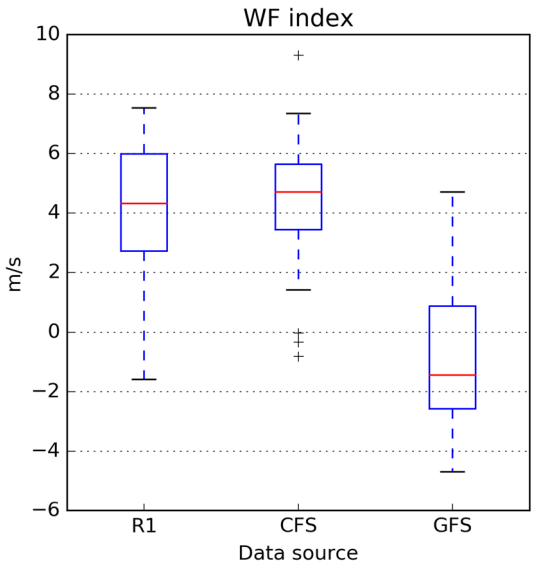

Fig. 17 Box-and-whisker diagram for the EASM's WF index (Wang and Fan 1999) obtained from its inter-annual time series of JJA mean field (1949–2008) of R1, CFS run, and GFS run. The bottom and top of the box are the first and third quartiles, and the band inside the box is the second quartile (the median). The ends of the whiskers represent 1.5 interquartile range (IQR) of the lower and higher quartiles. Outliers plotted as individual points marked as "+"

Acknowledgements The authors thank anonymous reviewers for providing valuable comments. This material is based upon work supported by the National Science Foundation under Grant no. AGS-1419526. The authors acknowledge the Texas Advanced Computing Center (TACC) at The University of Texas at Austin (URL: http://www.tacc.utexas.edu) for providing High-Performance Computing (HPC) resources that have contributed to the research results reported within this paper. The work of K. Sperber, P. Gleckler, and (in part) J. Lee was performed under the auspices of the US Department of Energy by Lawrence Livermore National Laboratory under Contract DE-AC52-07NA27344. The efforts of these 3 authors are supported by the Regional and Global Climate Modeling Program of the United States Department of Energy's Office of Science. The CMAP precipitation data were provided by the NOAA/OAR/ESRL PSD, Boulder, Colorado, USA, from their website at http://www.esrl.noaa.gov/psd/. The OAFlux data were provided by the WHOI OAFlux project (http://oaflux.whoi.edu) funded by the NOAA Climate Observations and Monitoring (COM) program. The simulation result of this study is open to public upon request to authors, and we welcome other research groups to use the data to comprehensively analyze the impact on other regions.

References

Arakawa A (2000) A personal perspective of the early years of general circulation modeling at UCLA. In: Randall DA (ed) General circulation model development: past, present, and future. Proceedings of a symposium in Honor of Professor Akio Arakawa. Academic Press, New York, pp 1–65

Bombardi RJ, Schneider EK, Marx L, Halder S, Singh B, Tawfik AB, Dirmeyer PA, Kinter JL (2015a) Improvements in the representation of the Indian summer monsoon in the NCEP climate forecast system version 2. Clim Dyn 45:2485–2498

Bombardi RJ, Zhu J, Marx L, Huang B, Chen H, Lu J, Krishnamurthy L, Krishnamurthy V, Colfescu I, Kinter JL, Kumar A, Hu ZZ, Moorthi S, Tripp P, Wu X, Schneider EK (2015b) Evaluation of the CFSv2 CMIP5 decadal predictions. Clim Dyn 44:543–557

Bonfils C, Santer BD (2011) Investigating the possibility of a human component in various pacific decadal oscillation indices. Clim Dyn 37:1457–1468. https://doi.org/10.1007/s00382-010-0920-1

Bonfils CJW, Santer BD, Phillips TJ, Marvel K, Ruby Leung L, Doutriaux C, Capotondi A (2015) Relative contributions of mean-state shifts and ENSO-driven variability to precipitation changes in a warming climate. J Clim 28:9997–10013. https://doi.org/10.1175/JCLI-D-15-0341.1

Cook KH, Vizy EK (2006) Coupled model simulations of the West African monsoon system: twentieth- and twenty-first century simulations. J Clim 19:3681–3703

De Sales F, Xue Y (2013) Dynamic downscaling of 22-year CFS winter seasonal hindcasts with the UCLA-ETA regional climate model over the United States. Clim Dyn 41:255–275

Devanand A, Roxy MK, Ghosh S (2018) Coupled land-atmosphere regional model reduces dry bias in Indian summer monsoon rainfall simulated by CFSv2. Geophys Res Lett 45:2476–2486

Diallo I, Bain CL, Gaye AT, Moufouma-Okia W, Niang C, Dieng MDB, Graham R (2014) Simulation of the West African monsoon onset using the HadGEM3-RA regional climate model. Clim Dyn 43:575–594. https://doi.org/10.1007/s00382-014-2219-0

Diallo I, Giorgi F, Sukumaran S, Stordal F, Giuliani G (2015) Evaluation of RegCM4 driven by CAM4 over Southern Africa: mean climatology, interannual variability and daily extremes of wet season temperature and precipitation. Theor Appl Climatol 121:749–766. https://doi.org/10.1007/s00704-014-1260-6

Ding Y, Wang Z, Sun Y (2008) Inter-decadal variation of the summer precipitation in East China and its association with decreasing Asian summer monsoon. Part I: observed evidences. Int J Climatol 28:1139–1161. https://doi.org/10.1002/joc.1615

Dong X, Lin R, Zhu J, Lu Z (2016) Evaluation of ocean data assimilation in CAS-ESM-C: constraining the SST field. Adv Atmos Sci 33:795–807

Dong B, Sutton RT, Shaffrey L, Klingaman NP (2017) Attribution of forced decadal climate change in coupled and uncoupled ocean–atmosphere model experiments. J Clim 30:6203–6223

Ek MB, Mitchell KE, Lin Y, Rogers E, Grunmann P, Koren V, Gayno G, Tarpley JD (2003) Implementation of Noah land surface model advances in the National Centers for Environmental Prediction operational mesoscale Eta model. J Geophys Res 108:8851. https://doi.org/10.1029/2002JD003296

Eyring V, Bony S, Meehl GA, Senior CA, Stevens B, Stouffer RJ, Taylor KE (2016) Overview of the Coupled Model Intercomparison Project Phase 6 (CMIP6) experimental design and organization. Geosci Model Dev 9:1937–1958

Fan Y, van den Dool H (2008) A global monthly land surface air temperature analysis for 1948–present. J Geophys Res 113:D01103

Fu J, Li S, Luo D (2009) Impact of global SST on decadal shift of East Asian summer climate. Adv Atmos Sci 26:192–201

García-Serrano J, Doblas-Reyes FJ, Haarsma RJ, Polo I (2013) Decadal prediction of the dominant West African monsoon rainfall modes. J Geophys Res Atmos 118:5260–5279. https://doi.org/10.1002/jgrd.50465

Gates WL (1992) AMIP: the atmospheric model intercomparison project. Bull Am Meteorol Soc 73:1962–1970

Goswami BN, Madhusoodanan MS, Neema CP, Sengupta D (2006) A physical mechanism for North Atlantic SST influence on the Indian summer monsoon. Geophys Res Lett 33:L02706

Goswami BB, Deshpande M, Mukhopadhyay P, Saha SK, Rao SA, Murthugudde R, Goswami BN (2014) Simulation of monsoon intraseasonal variability in NCEP CFSv2 and its role on systematic bias. Clim Dyn 43:2725–2745

Gottschalck J, Wheeler M, Weickmann K, Vitart F, Savage N, Lin H, Hendon H, Waliser D, Sperber K, Nakagawa M, Prestrelo C, Flatau M, Higgins W (2010) A framework for assessing operational Madden–Julian oscillation forecasts: a CLIVAR MJO working group project. Bull Am Meteorol Soc 91:1247–1258. https://doi.org/10.1175/2010BAMS2816.1

Griffies SM, Harrison MJ, Pacanowski RC, Rosati A (2004) A technical guide to MOM4. GFDL Ocean Group Tech Rep 5. https://www.gfdl.noaa.gov/bibliography/related_files/smg0301.pdf. Accessed 20 Nov 2017

Gu Y, Xue Y, De Sales F, Liou KN (2016) A GCM investigation of dust aerosol impact on the regional climate of North Africa and South/East Asia. Clim Dyn 46:2353–2370

Gu Y, Liou KN, Jiang JH, Fu R, Lu S, Xue Y (2017) A GCM investigation of impact of aerosols on the precipitation in Amazon during the dry to wet transition. Clim Dyn 48:2393–2404

Guo L, Highwood EJ, Shaffrey LC, Turner AG (2013) The effect of regional changes in anthropogenic aerosols on rainfall of the East Asian Summer Monsoon. Atmos Chem Phys 13:1521–1534

Ha KJ, Heo KY, Lee SS, Yun KS, Jhun JG (2012) Variability in the East Asian monsoon: a review. Meteorol Appl 19:200–215

Ham S, Hong SY, Park S (2014) A study on air–sea interaction on the simulated seasonal climate in an ocean-atmosphere coupled model. Clim Dyn 42:1175–1187

Han W, Vialard J, McPhaden MJ, Lee T, Masumoto Y, Feng M, De Ruijter WP (2014) Indian Ocean decadal variability: a review. Bull Am Meteorol Soc 95:1679–1703

Harris I, Jones PD, Osborn TJ, Lister DH (2014) Updated high-resolution grids of monthly climatic observations—the CRU TS3.10 dataset. Int J Climatol 34:623–642. https://doi.org/10.1002/joc.3711

Hong SY, Park H, Cheong HB, Kim JEE, Koo MS, Jang J, Ham S, Hwang SO, Park BK, Chang EC, Li H (2013) The global/regional integrated model system (GRIMs). Asia Pac J Atmos Sci 49:219–243

Huang B, Zhu J, Marx L, Wu X, Kumar A, Hu ZZ, Balmaseda MA, Zhang S, Lu J, Schneider EK, Kinter JL III (2015) Climate drift of AMOC, North Atlantic salinity and arctic sea ice in CFSv2 decadal predictions. Clim Dyn 44:559–583

Hwang YT, Frierson DM (2013) Link between the double-Intertropical Convergence Zone problem and cloud biases over the Southern Ocean. Proc Natl Acad Sci USA 110:4935–4940

Infanti MJ, Kirtman BP (2017) CGCM and AGCM seasonal climate predictions: a study in CCSM4. J Geophys Res Atmos 122:7416–7423

Jiang X, Yang S, Li Y, Kumar A, Liu X, Zuo Z, Jha B (2013) Seasonal-to-interannual prediction of the Asian summer monsoon in the NCEP climate forecast system version 2. J Clim 26:3708–3727

Kalnay E, Kanamitsu M, Kistler R, Collins W, Deaven D, Gandin L, Iredell M, Saha S, White G, Woollen J, Zhu Y, Leetmaa A, Reynolds R, Chelliah M, Ebisuzaki W, Higgins W, Janowiak J, Mo KC, Ropelewski C, Wang J, Jenne R, Joseph D (1996) The NCEP/NCAR 40-year reanalysis project. Bull Am Meteorol Soc 77:437–471. https://doi.org/10.1175/1520-0477(1996)077%3C0437:TNYRP%3E2.0.CO;2

Kang I-S, Jin K, Wang B, Lau K-M, Shukla J, Krishnamurthy V, Schubert SD, Wailser DE, Stern WF, Kitoh A, Meehl GA, Kanamitsu M, Galin VY, Satyan V, Park C-K, Liu Y (2002) Intercomparison of the climatological variations of Asian summer monsoon precipitation simulated by 10 GCMs. Clim Dyn 19:383–395

Kang H-S, Xue Y, Collatz GJ (2007) Assessment of satellite-derived leaf area index datasets using a general circulation model: seasonal variability. J Clim 20:993–1015

Kim HM, Webster PJ, Curry JA (2012a) Evaluation of short-term climate change prediction in multi-model CMIP5 decadal hindcasts. Geophys Res Lett 39:L10701. https://doi.org/10.1029/2012GL051644

Kim HM, Webster PJ, Curry JA, Toma VE (2012b) Asian summer monsoon prediction in ECMWF system 4 and NCEP CFSv2 retrospective seasonal forecasts. Clim Dyn 39:2975–2991

Klein SA, Jiang X, Boyle J, Malyshev S, Xie S (2006) Diagnosis of the summertime warm and dry bias over the US Southern Great Plains in the GFDL climate model using a weather forecasting approach. Geophys Res Lett 33:L18805. https://doi.org/10.1029/2006GL027567

Köhl A (2015) Evaluation of the GECCO2 ocean synthesis: transports of volume, heat and freshwater in the Atlantic. QJR Meteorol Soc 141:166–181. https://doi.org/10.1002/qj.2347

Krishnamurthy V (2017) Seasonal prediction of South Asian monsoon in CFSv2. Clim Dyn. https://doi.org/10.1007/s00382-017-3963-8

Krishnamurthy V (2018) Predictability of CFSv2 in the tropical Indo-Pacific region, at daily and subseasonal time scales. Clim Dyn 50:3931–3948. https://doi.org/10.1007/s00382-017-3855-y

Krishnan R, Sugi M (2003) Pacific decadal oscillation and variability of the Indian summer monsoon rainfall. Clim Dyn 21:233–242

Kug J-S, Kang I-S, Choi D-H (2008) Seasonal climate predictability with tier-one and tier-two prediction systems. Clim Dyn 31:403–416

Kumar A, Wang H (2015) On the potential of extratropical SST anomalies for improving climate predictions. Clim Dyn 44:2557–2569

Lee JY, Wang B (2014) Future change of global monsoon in the CMIP5. Clim Dyn 42:101–119. https://doi.org/10.1007/s00382-012-1564-0

Lee JY, Kwon M, Yun KS, Min SK, Park IH, Ham YG, Jin EK, Kim JH, Seo KH, Kim W, Yim SY (2017) The long-term variability of Changma in the East Asian summer monsoon system: a review and revisit. Asia Pac J Atmos Sci 53:257–272

Lee J, Sperber K, Gleckler P, Bonfils C, Taylor KE (2018) Quantifying the agreement between observed and simulated leading modes of extratropical interannual variability. Clim Dyn **(in revision)**

Lei Y, Hoskins B, Slingo J (2011) Exploring the interplay between natural decadal variability and anthropogenic climate change in summer rainfall over China. Part I: observational evidence. J Clim 24:4584–4599

Li G, Xie SP (2014) Tropical biases in CMIP5 multimodel ensemble: the excessive equatorial Pacific cold tongue and double ITCZ problems. J Clim 27:1765–1780

Li C, He J, Zhu J (2004) A review of decadal/interdecadal climate variation studies in China. Adv Atmos Sci 21:425–436

Lin JL (2007) The double-ITCZ problem in IPCC AR4 coupled GCMs: ocean–atmosphere feedback analysis. J Clim 20:4497–4525

Lin R, Zhu J, Zheng F (2016) Decadal shifts of East Asian summer monsoon in a climate model free of explicit GHGs and aerosols. Sci Rep 6:38546. https://doi.org/10.1038/srep38546

Ma HY, Mechoso CR, Xue Y, Xiao H, Wu CM, Li JL, De Sales F (2011) Impact of land surface processes on the South American warm season climate. Clim Dyn 37:187–203

Ma HY, Xiao H, Mechoso CR, Xue Y (2013a) Sensitivity of global tropical climate to land surface processes: mean state and interannual variability. J Clim 26:1818–1837

Ma HY, Mechoso CR, Xue Y, Xiao H, Neelin JD, Ji X (2013b) On the connection between continental-scale land surface processes and the tropical climate in a coupled ocean–atmosphere–land system. J Clim 26:9006–9025

Ma HY, Xie S, Klein SA, Williams KD, Boyle JS, Bony S, Douville H, Fermepin S, Medeiros B, Tyteca S, Watanabe M (2014) On the correspondence between mean forecast errors and climate errors in CMIP5 models. J Clim 27:1781–1798

Mechoso CR, Yu JY, Arakawa A (2000) A coupled GCM pilgrimage: from climate catastrophe to ENSO simulations. In: Randall DA (ed) General circulation model development: past, present, and future. Proceedings of a symposium in Honor of Professor Akio Arakawa. Academic Press, New York, pp 539–575

Meehl GA, Covey C, Taylor KE, Delworth T, Stouffer RJ, Latif M, McAvaney B, Mitchell JF (2007) The WCRP CMIP3 multimodel dataset: a new era in climate change research. Bull Am Meteorol Soc 88:1383–1394

Meehl GA, Goddard L, Murphy J, Stouffer RJ, Boer G, Danabasoglu G, Dixon K, Giorgetta MA, Greene AM, Hawkins ED, Hegerl G (2009) Decadal prediction: can it be skillful? Bull Am Meteorol Soc 90:1467–1485

Mo KC, Shukla S, Lettenmaier DP, Chen LC (2012) Do Climate Forecast System (CFSv2) forecasts improve seasonal soil moisture prediction? Geophys Res Lett 39:L23703. https://doi.org/10.1029/2012GL053598

Mohan TS, Annamalai H, Marx L, Huang B, Kinter J (2018) Representation of ocean–atmosphere processes associated with extended monsoon episodes over South Asia in CFSv2. Front Earth Sci 6:9. https://doi.org/10.3389/feart.2018.00009

Mohino E, Janicot S, Bader J (2011) Sahel rainfall and decadal to multi-decadal sea surface temperature variability. Clim Dyn 37:419–440

Oueslati B, Bellon G (2015) The double ITCZ bias in CMIP5 models: interaction between SST, large-scale circulation and precipitation. Clim Dyn 44:585–607

Paeth H, Paxian A, Sein D, Jacob D, Panitz HJ, Warscher M, Fink A, Kunstmann H, Breil M, Engel T, Krause A (2017) Decadal and multi-year predictability of the West African monsoon and the role of dynamical downscaling. Meteorol Z 26:363–377

Pillai PA, Rao SA, Das RS, Salunke K, Dhakate A (2017) Potential predictability and actual skill of Boreal Summer Tropical SST and Indian summer monsoon rainfall in CFSv2-T382: role of initial SST and teleconnections. Clim Dyn. https://doi.org/10.1007/s00382-017-3936-y

Pokhrel S, Rahaman H, Parekh A, Saha SK, Dhakate A, Chaudhari HS, Gairola RM (2012) Evaporation–precipitation variability over Indian Ocean and its assessment in NCEP Climate Forecast System (CFSv2). Clim Dyn 39:2585–2608

Pokhrel S, Saha SK, Dhakate A, Rahman H, Chaudhari HS, Salunke K, Hazra A, Sujith K, Sikka DR (2016) Seasonal prediction of Indian summer monsoon rainfall in NCEP CFSv2: forecast and predictability error. Clim Dyn 46:2305–2326

Richter I, Xie S-P (2008) On the origin of equatorial Atlantic biases in coupled general circulation models. Clim Dyn 31:587–598. https://doi.org/10.1007/s00382-008-0364-z

Rodríguez-Fonseca B, Janicot S, Mohino E, Losada T, Bader J, Caminade C, Chauvin F, Fontaine B, García-Serrano J, Gervois S, Joly M (2011) Interannual and decadal SST-forced responses of the West African monsoon. Atmos Sci Lett 12:67–74

Roehrig R, Bouniol D, Guichard F, Hourdin F, Redelsperger J-L (2013) The present and future of the West African monsoon: a process-oriented assessment of CMIP5 simulations along the AMMA transect. J Clim 26:6471–6505. https://doi.org/10.1175/JCLI-D-12-00505.1

Rowell DP, Folland CK, Maskell K, Ward MN (1995) Variability of summer rainfall over tropical North Africa (1906–92): observations and modelling. Q J R Meteorol Soc 121:669–704

Saha S, Nadiga S, Thiaw C, Wang J, Wang W, Zhang Q, Van den Dool HM, Pan HL, Moorthi S, Behringer D, Stokes D (2006) The NCEP climate forecast system. J Clim 19:3483–3517

Saha S, Moorthi S, Pan HL, Wu X, Wang J, Nadiga S, Tripp P, Kistler R, Woollen J, Behringer D, Liu H (2010) The NCEP climate forecast system reanalysis. Bull Am Meteorol Soc 91:1015–1057. https://doi.org/10.1175/2010BAMS3001.1

Saha S, Moorthi S, Wu X, Wang J, Nadiga S, Tripp P, Behringer D, Hou YT, Chuang HY, Iredell M, Ek M (2014) The NCEP climate forecast system version 2. J Clim 27:2185–2208. https://doi.org/10.1175/JCLI-D-12-00823.1

Sahai AK, Chattopadhyay R, Joseph S, Mandal R, Dey A, Abhilash S, Krishna RP, Borah N (2015) Real-time performance of a multi-model ensemble-based extended range forecast system in predicting the 2014 monsoon season based on NCEP-CFSv2. Curr Sci 109:1802–1813

Shin CS, Huang B (2016) Slow and fast annual cycles of the Asian summer monsoon in the NCEP CFSv2. Clim Dyn 47:529–553

Shukla RP, Kinter JL (2015) Simulations of the Asian monsoon using a regionally coupled-global model. Clim Dyn 44:827–843. https://doi.org/10.1007/s00382-014-2188-3

Silva GA, Dutra LM, da Rocha RP, Ambrizzi T, Leiva É (2014) Preliminary analysis on the global features of the NCEP CFSv2 seasonal hindcasts. Adv Meteorol 2014:695067. https://doi.org/10.1155/2014/695067

Song F, Zhang GJ (2016) Effects of southeastern Pacific sea surface temperature on the double-ITCZ bias in NCAR CESM1. J Clim 29:7417–7433

Song F, Zhou T (2014) The climatology and interannual variability of East Asian summer monsoon in CMIP5 coupled models: does air–sea coupling improve the simulations? J Clim 27:8761–8777

Sperber KR (2004) Madden–Julian variability in NCAR CAM2.0 and CCSM2.0. Clim Dyn 23:259–278. https://doi.org/10.1007/s00382-004-0447-4

Sperber KR, Annamalai H (2008) Coupled model simulations of boreal summer intraseasonal (30–50 day) variability, part 1: systematic errors and caution on use of metrics. Clim Dyn 31:345–372. https://doi.org/10.1007/s00382-008-0367-9

Sperber KR, Gualdi S, Legutke S, Gayler V (2005) The Madden–Julian oscillation in ECHAM4 coupled and uncoupled general circulation models. Clim Dyn 25:117–140. https://doi.org/10.1007/s00382-005-0026-3

Sperber KR, Annamalai H, Kang IS, Kitoh A, Moise A, Turner A, Wang B, Zhou T (2013) The Asian summer monsoon: an intercomparison of CMIP5 vs. CMIP3 simulations of the late 20th century. Clim Dyn 41:2711–2744. https://doi.org/10.1007/s00382-012-1607-6

Swapna P, Roxy MK, Aparna K, Kulkarni K, Prajeesh AG, Ashok K, Krishnan R, Moorthi S, Kumar A, Goswami BN (2015) The IITM earth system model: transformation of a seasonal prediction model to a long-term climate model. Bull Am Meteorol Soc 96:1351–1367

Taylor KE, Stouffer RJ, Meehl GA (2012) An overview of CMIP5 and the experiment design. Bull Am Meteorol Soc 93:485–498. https://doi.org/10.1175/BAMS-D-11-00094.1

Von Storch H, Zwiers FW (1999) Statistical analysis in climate research. Cambridge University Press, Cambridge

Wang B, Ding Q (2006) Changes in global monsoon precipitation over the past 56 years. Geophys Res Lett 33:L06711. https://doi.org/10.1029/2005GL025347

Wang B, Fan Z (1999) Choice of South Asian summer monsoon indices. Bull Am Meteorol Soc 80:629–638

Wang B, Kang IS, Lee J-Y (2004) Ensemble simulations of Asian–Australian monsoon variability by 11 AGCMs. J Clim 17:803–818

Wang B, Ding Q, Fu X, Kang I-S, Jin K, Shukla J, Doblas-Reyes F (2005) Fundamental challenge in simulation and prediction of summer monsoon rainfall. Geophys Res Lett 32:L15711. https://doi.org/10.1029/2005GL022734

Wang B, Wu Z, Li J, Liu J, Chang C-P, Ding Y, Wu G (2008) How to measure the strength of the East Asian summer monsoon. J Clim 21:4449–4463

Wang H, Xie X, Liu X (2015) On the robustness of the weakening effect of anthropogenic aerosols on the East Asian summer monsoon with multimodel results. Adv Meteorol 2015:397395. https://doi.org/10.1155/2015/397395

Wheeler MC, Hendon HH (2004) An all-season real-time multivariate MJO index: development of an index for monitoring and prediction. Mon Weather Rev 132:1917–1932

Wu R, Kirtman BP, Pigion K (2007) Surface latent heat flux and its relationship with sea surface temperature in the National Centers for Environmental Prediction Climate Forecast System simulations and retrospective forecasts. Geophys Res Lett 34:L17712. https://doi.org/10.1029/2007GL030751

Xie P, Arkin PA (1997) Global precipitation: a 17-year monthly analysis based on gauge observations, satellite estimates, and numerical model outputs. Bull Am Meteorol Soc 78:2539–2558

Xue Y, Sellers PJ, Kinter JL, Shukla J (1991) A simplified biosphere model for global climates studies. J Clim 4:345–2364

Xue Y, Juang HM, Li W, Prince S, DeFries R, Jiao Y, Vasic R (2004) Role of land surface processes in monsoon development: East Asia and West Africa. J Geophys Res 109:D03105. https://doi.org/10.1029/2003JD003556

Xue Y, Ji J, Sun S, Wu G, Lau KM, Poccard I, Kang HS, Zhang R, Schaake JC, Zhang JY, Jiao Y (2005) Multiscale variability of the river runoff system in China and its link to precipitation and sea surface temperature. J Hydrometeorol 6:550–570

Xue Y, De Sales F, Li W-P, Mechoso CR, Nobre CA, Juang H-M (2006) Role of land surface processes in South American monsoon development. J Clim 19:741–762

Xue Y, De Sales F, Vasic R, Mechoso CR, Arakawa A, Prince S (2010) Global and seasonal assessment of interactions between climate and vegetation biophysical processes: a GCM study with different land–vegetation representations. J Clim 23:1411–1433

Xue Y, De Sales F, Lau WK, Boone A, Kim KM, Mechoso CR, Wang G, Kucharski F, Schiro K, Hosaka M, Li S, Druyan LM, Seidou Sanda I, Thiaw W, Zeng N, Comer RE, Lim YK, Mahanama S, Song G, Gu Y, Hagos SM, Chin M, Schubert S, Dirmeyer P, Leung LR, Kalnay E, Kitoh A, Lu CH, Mahowald NM, Zhang Z (2016a) West African monsoon decadal variability and drought and surface-related forcings: second West African Monsoon Modeling and Evaluation Project Experiment (WAMME II). Clim Dyn 47:3517–3545

Xue Y, Oaida CM, Diallo I, Neelin JD, Li S, De Sales F, Gu Y, Robinson DA, Vasic R, Yi L (2016b) Spring land temperature anomalies in northwestern US and the summer drought over Southern Plains and adjacent areas. Environ Res Lett 11:044018. https://doi.org/10.1088/1748-9326/11/4/044018

Yim SY, Wang B, Kwon M (2014) Interdecadal change of the controlling mechanisms for East Asian early summer rainfall variation around the mid-1990s. Clim Dyn 42:1325–1333

Yoon JH, Mo K, Wood EF (2012) Dynamic-model-based seasonal prediction of meteorological drought over the contiguous United States. J Hydrometeorol 13:463–482

Yu L, Weller RA (2007) Objectively analyzed air–sea heat fluxes for the global ice-free oceans (1981–2005). Bull Am Meteorol Soc 88:527–539

Yuan X, Wood EF, Luo L, Pan M (2011) A first look at Climate Forecast System version 2 (CFSv2) for hydrological seasonal prediction. Geophys Res Lett 38:L13402. https://doi.org/10.1029/2011GL047792

Yuan X, Wood EF, Roundy JK, Pan M (2013) CFSv2-based seasonal hydroclimatic forecasts over the conterminous United States. J Clim 26:4828–4847

Zhan X, Xue Y, Collatz GJ (2003) An analytical approach for estimating CO_2 and heat fluxes over the Amazonian region. Ecol Model 162:97–117

Zhang X, Liu H, Zhang M (2015) Double ITCZ in coupled ocean-atmosphere models: from CMIP3 to CMIP5. Geophys Res Lett 42:8651–8659. https://doi.org/10.1002/2015GL065973

Zhang C, Xie S, Klein SA, Ma HY, Tang S, Weverberg KV, Morcrette CJ, Petch J (2018) CAUSES: diagnosis of the summertime warm bias in CMIP5 climate models at the ARM southern great plains site. J Geophys Res Atmos. https://doi.org/10.1002/2017JD027200 **(accepted)**

Zheng J, Wu M, Ge Q, Hao Z, Zhang X (2017) Observed, reconstructed, and simulated decadal variability of summer precipitation over eastern China. J Meteorol Res Prc 31:49–60

Zhou J, Lau KM (2001) Principal modes of interannual and decadal variability of summer rainfall over South America. Int J Climatol 21:1623–1644

Zhou T, Gong D, Li J, Li B (2009) Detecting and understanding the multi-decadal variability of the East Asian Summer Monsoon—recent progress and state of affairs. Meteorol Z 18:455–467. https://doi.org/10.1127/0941-2948/2009/0396

Zou L, Zhou T (2013) Can a regional ocean–atmosphere coupled model improve the simulation of the interannual variability of the Western North Pacific summer monsoon? J Clim 26:2353–2367. https://doi.org/10.1175/JCLI-D-11-00722.1